This article has been accepted for inclusion in a future issue of this journal. Content is final as presented, with the exception of pagination.

Robust CFAR Detector Based on Truncated Statistics in Multiple-Target Situations

Ding Tao, Stian Normann Anfinsen, *Member, IEEE*, and Camilla Brekke, *Member, IEEE*

***Abstract*—A new and robust constant false alarm rate (CFAR) detector based on truncated statistics (TSs) is proposed for ship detection in single-look intensity and multilook intensity synthetic aperture radar data. The approach is aimed at high-target-density situations such as busy shipping lines and crowded harbors, where the background statistics are estimated from potentially contaminated sea clutter samples. The CFAR detector uses truncation to exclude possible statistically interfering outliers and TSs to model the remaining background samples. The derived truncated statistic CFAR (TS-CFAR) algorithm does not require prior knowledge of the interfering targets. The TS-CFAR detector provides accurate background clutter modeling, a stable false alarm regulation property, and improved detection performance in high-target-density situations.**

***Index Terms*—Constant false alarm rate (CFAR), sea clutter, statistical modeling, synthetic aperture radar (SAR), target detection, truncated statistics (TSs).**

I. Introduction

SYNTHETIC aperture radar (SAR) provides valuable measurements of the Earth surface for many remote sensing applications, whereof maritime target detection is one common field of use. The well-known constant false alarm rate (CFAR) target detectors adaptively determine the detection threshold based on accurate modeling of the statistical distribution of local background clutter measurements.[1] They are often implemented with the sliding window technique, and the parameters of the hypothesized model are estimated within this local reference window. In practice, however, heterogeneous clutter and interfering targets can often lead to inaccurate estimation and deceptive modeling. Clutter edges and transitions in clutter intensity due to meteorological and oceanographic phenomena is one common cause of heterogeneity, and the effects can be suppressed by utilizing advanced background estimation algorithms [1]–[3]. Another problem is statistical contamination when the sliding window contains one or more interfering targets, which can result in severe degradation of the CFAR detector performance. The latter case is the focus of this paper.

Manuscript received April 14, 2014; revised October 22, 2014 and June 4, 2015; accepted June 26, 2015.

The authors are with the Department of Physics and Technology, University of Tromsø-The Arctic University of Norway, 9037 Tromsø, Norway (e-mail: tao.ding@uit.no; stian.normann.anfinsen@uit.no; camilla.brekke@uit.no).

Color versions of one or more of the figures in this paper are available online at http://ieeexplore.ieee.org.

Digital Object Identifier 10.1109/TGRS.2015.2451311

[1]The term *clutter* is used in this paper exclusively about backscatter from the sea, which is also referred to as the *background*, and not about measurements that contain energy from any target.

The aim of this paper is to derive a robust CFAR algorithm that excludes statistical contamination in the reference window that may occur in dense target situations, such as busy shipping lines and crowded harbors, and, in a statistically rigorous manner, to model the remaining sea clutter samples. In general, a raised detection threshold results when there is one or more unwanted outliers in the reference window in the form of nonoceanic targets and their sidelobes, or ghosts. This causes the observed probability of false alarms to drop below the specified value and lowers the probability of detection, which is known as the *capture effect* [4]–[7]. From previous studies [3], [7]–[14], the primary solution is to remove the outliers, encompassing both interfering targets and naturally occurring spikes in the sea clutter, from the background samples, or to represent the background clutter by a statistic that is less influenced by the outliers. Outlier removal is usually done by data ranking or censoring with different restrictions. This paper proposes a new approach based on data truncation, which employs a statistically rigorous analysis of the truncated data. The important distinction between censoring and truncation will be highlighted after our review of the literature on CFAR detectors. This review follows after we have defined some key terms.

In the paper, we distinguish between clutter pixels and target pixels. The term "clutter" is used for any radar measurement of an ocean surface that is not affected by a target. Hence, clutter can be interpreted as equivalent of background, consisting of backscatter from a natural ocean surface. The measurements of clutter and targets can, in principle, be modeled by respective statistical distributions. For instance, the gamma distribution will be assumed as a parametric model for homogeneous clutter, meaning clutter from an area with constant radar reflectivity. It is considered, on the other hand, that the target distribution cannot be identified because of the variable characteristics of potential targets and the unknown influence of viewing angles and target orientation. Next, an outlier is defined as a measurement that stands out by its high intensity. It can be either a clutter realization from the tail of clutter distribution or a measurement of target plus clutter. Since the target distribution is unknown, ship detection is performed by identifying outliers with respect to the clutter distribution. The threshold is determined by the CFAR approach.

The traditional cell-averaging CFAR (CA-CFAR) detector [15] represents the background data by an average over the reference window and assumes a homogeneous clutter environment. Its variations include the greatest-of CFAR (GO-CFAR) [2] and the smallest-of CFAR (SO-CFAR) [1] detectors, which divide the reference window in spatial subsets before averaging. The GO-CFAR detector represents the clutter by the greatest

0196-2892 © 2015 IEEE. Personal use is permitted, but republication/redistribution requires IEEE permission.
See http://www.ieee.org/publications_standards/publications/rights/index.html for more information.

This article has been accepted for inclusion in a future issue of this journal. Content is final as presented, with the exception of pagination.

of the subset mean values and the SO-CFAR detector by the smallest. They deliver improved performance when the reference window contains clutter intensity transitions or multiple targets, respectively. In homogeneous clutter, the former suffers a loss in detection rate and the latter an increased false alarm rate [3]. In a different manner, the variability index CFAR (VI-CFAR) detector [3] dynamically selects the particular group of reference pixels to estimate clutter statistics. The VI is a test statistic that is used to choose between the CA-CFAR, GO-CFAR, and SO-CFAR approaches. The VI-CFAR detector robustly performs in all the common test cases, but it is subject to inevitable performance loss when the clutter heterogeneities have a complex distribution that cannot be handled by the simple spatial subsetting scheme.

The ordered statistic CFAR (OS-CFAR) detector is another well-known CFAR algorithm that has been studied to deal with interfering outliers within the reference window [9]. The OS-CFAR detector rank-orders the background pixel measurements based on their magnitude. The parameters of the hypothesized model are estimated from a single value selected from the ordered sequence. This value, known as an order statistic, is more robust to outliers than the mean but provides slightly less information for estimation purposes. Hence, the OS-CFAR detector suffers a small loss in detection rate in homogeneous clutter relative to the CA-CFAR but maintains a significantly higher detection rate and a false alarm rate closer to the specified value in multiple-target situations [16]. The improvement comes at a higher computational cost. The trimmed mean CFAR (TM-CFAR) detector was introduced in [11] as a generalization of the OS-CFAR detector and uses the mean of a set of rank-ordered values to estimate distribution parameters. It has been shown to robustly perform only after prior assessment of the interfering environment [17], and optimal performance relies on a judicious choice of the trimming parameters [18]. It notably contains both the CA-CFAR detector and the OS-CFAR detector as special cases, which are included in the experiments and comparisons of the paper.

The OS-CFAR and TM-CFAR detectors represent a strategy of radiometric subsetting of the reference window. To extract a subset, the pixel values must first be ranked. The subsetting strategy reflects the particular clutter situation that the method is aimed at. In addition, there are many hybrid CFAR detectors designed to accommodate several clutter environments in one algorithm. These incorporate different strategies and dynamically activate the appropriate one. One example is the censored mean-level detector (CMLD) [8], which employs both ranking and censoring techniques to obtain acceptable performance in the presence of interfering targets. It excludes the largest reference samples and uses the remaining samples in the parameter estimation. It suffers some detection loss in a homogeneous environment and is quite robust in multiple-target situations, as long as all interfering targets are removed from the reference clutter [19]. However, without prior knowledge of the interfering targets, the CMLD may lose its robustness and CFAR properties [6]. Many more hybrid algorithms may be found, e.g., the automatic CMLD, the generalized two-level CMLD [7], and the automatic censored CA-CFAR detector based on ordered data variability [12], [17], [20], [21]. We do not include any hybrid detectors in the experiments. The reason is that we focus only on the multiple-target situation and also because we want to test one single strategy at a time to provide a simple and clear comparative study. Different strategies can always be combined at a later stage in a more advanced algorithm.

A different approach to the multiple-target situation is the iterative censoring (IC) scheme proposed by Barboy *et al.* [10]. Samples that exceed an adaptive threshold are excluded here, and the threshold is iteratively updated based on the censored reference sample. This is repeated until there are no changes in the threshold and the reference sample, and the detection result has converged. In more recent articles [13], [14], a similar mechanism has been implemented by applying an iteratively updated map of outliers (potential targets). Although the multistep adaptive detection procedure may need many cycles and require long calculation time, the IC scheme has shown robust performance in the dense target situation and can be integrated with any CFAR algorithm. In this paper, we include the IC implementation of the CA-CFAR and OS-CFAR detectors in the comparison of methods. These are referred to as ICCA-CFAR and ICOS-CFAR, respectively, and represent, in our view, the state of the art in CFAR detection.

The final algorithm included in the comparison is the truncated statistic CFAR (TS-CFAR) detector, which is proposed here. First, note that truncation is similar to but distinct from censoring, and these terms sometimes have been used incorrectly in the target detection literature. Both in truncation and censoring, data points with a value outside specified thresholds are excluded from the sample or not observed. The difference is that the number of censored data points is recorded, whereas the number of truncated data points remains unknown. When high-intensity outliers are removed from a background sample, they consist of an indistinguishable mixture of target pixels and sea clutter spikes. Since we do not know how many target pixels there are among the outliers, the number of sea clutter measurements removed is effectively unknown. This categorizes the outlier removal as truncation with respect to the remaining sea clutter sample, thereby assuming that all target pixels have been removed. Truncation is therefore the relevant operation for statistical characterization of sea clutter in a multiple-target environment.

The distinction between censoring and truncation becomes important once we start to analyze the reduced sample (with outliers removed) in a statistically rigorous manner, i.e., when we model the reduced sample with a truncated distribution and deduce parameter estimators from this model. A common simplifying practice has been to maintain the original model assumption also after outliers have been removed and to apply standard estimators derived for the untruncated distribution to the reduced sample, which must clearly produce wrong results. Specifically, a location or scale parameter is inevitably underestimated after high-intensity outliers (including all targets) have been removed, unless this is accounted for in the model and consequently compensated within the estimator. Hence, apart from correcting the terminology, we also address another malpractice in the literature: From the perspective of statistical modeling, the truncated data should be represented by truncated versions of the hypothesized distribution.

This article has been accepted for inclusion in a future issue of this journal. Content is final as presented, with the exception of pagination.

In this paper, the truncated exponential and the truncated gamma distributions are proposed to model the truncated samples of single-look intensity (SLI) and multilook intensity (MLI) SAR measurements. TS-CFAR algorithms are derived to handle truncated data in a statistically rigorous manner and to improve detection performance. The assumption underlying these models for the SLI and MLI data is that the signal variation stems from fully developed speckle and that the radar cross section is locally stationary. It is well known that this assumption may be violated as the sensor resolution increases and the sea becomes rough. Hence, more advanced models such as the K-distribution or the Weibull distribution may be called for. We nevertheless maintain this distributional assumption since they make it mathematically tractable to develop the truncated statistics (TSs) approach to CFAR detection. The extension to more advanced distributions is deferred until later. Moreover, our scope is the high-target-density situation and not high resolution or rough sea. We therefore assume that the exponential and gamma distributions will provide an adequate fit to the SLI and MLI data, respectively.

This paper is organized as follows. Section II provides an introduction to TSs and derives the proposed TS-CFAR detectors for both the exponentially distributed SLI and the gamma distributed MLI measurements of sea clutter. The usefulness of TS is demonstrated by showing the loss in parameter estimation accuracy caused by the presence of interfering targets. In Section III, the false alarm regulation property and the receiver operating characteristic (ROC) of the CFAR detector are examined based on simulated SLI and MLI measurements of sea clutter drawn from the exponential distribution and the gamma distribution, respectively. The TS-CFAR detector is compared with the conventional CA-CFAR and OS-CFAR detectors, whose IC schemes are also considered. Monte Carlo simulations are exploited in the analysis. The detection performance is then investigated in a comparative study in Section IV. Experiments are performed on data composited from real Radarsat-2 SAR measurements. Finally, Section V presents the main conclusions and perspectives.

II. TS-CFAR Detector

A. TSs

Outliers are data points that distinguish themselves from the main group of the data by their extreme values. In the context of SAR images and ship detection, these are measurements with unusually high intensity. Remark that we let the outlier term represent both strong returns from a natural sea surface, formed by constructive interference between oceanic scatterers, and the cases when a target return is superposed on the sea clutter. One of the main purposes when handling the possible occurrence of outliers is to find rigorous and robust methods to perform statistical inferences [22, Ch. 14]. The specific problem addressed here is parameter estimation in distribution models for SAR data when the sea clutter may be statistically contaminated by outliers. The proposed solution is to apply a truncation in order to eliminate possible contamination. The truncated data are then modeled with the truncated version of the statistical distribution hypothesized for the untruncated data.

Suppose we have a random variable X, which is distributed according to a probability density function (pdf) $p_X(x)$ and with a cumulative distribution function (cdf) $P_X(x)$. Let $\tilde{X}$ be the truncated version of X after applying a threshold t, which is called the *truncation depth*. A right truncated distribution can be defined as

$$p_{\tilde{X}}(x;t) = p_X(x \mid X < t) = \begin{cases} \frac{p_X(x)}{P_X(t)}, & 0 < x \leq t \\ 0, & x > t. \end{cases} \tag{1}$$

The normalization by $P_X(t)$ makes sure that $p_{\tilde{X}}(x;t)$ integrates to one. Note that the truncation depth is, in practice, a user-specified empirical value. It is difficult to estimate the optimal value from local statistics because of the lack of the knowledge about the location and the quantity of targets. Therefore, it is better to fix t to a value that ensures that all possible outliers are excluded, but be aware that excessive truncation may cause inaccurate parameter estimation of the distribution.

B. TS-CFAR Detector

In this section, CFAR detectors based on TS are derived for SLI and MLI SAR measurements, which are modeled by the exponential distribution and the gamma distribution, respectively [23]. The intensity measurements are greater than zero and assumed to be independent and identically distributed.

1) SLI: The SLI measurements are represented by X, which is assumed to follow the exponential distribution with pdf

$$p_X(x) = \frac{1}{\mu} e^{-x/\mu} \tag{2}$$

and cdf

$$P_X(x) = 1 - e^{-x/\mu} \tag{3}$$

where μ is the mean value. The truncated version of this pdf is derived as

$$p_{\tilde{X}}(x) = \begin{cases} \frac{p_X(x)}{P_X(t)} = \frac{1}{\mu} \frac{e^{-x/\mu}}{1-e^{-t/\mu}}, & 0 < x \leq t \\ 0, & x > t \end{cases} \tag{4}$$

where $P_X(t)$ is the exponential distribution cdf value at truncation depth t. The mean value is the only parameter that needs to be estimated. A maximum-likelihood (ML) estimator for the mean can be obtained from the likelihood function

$$\begin{aligned} \mathcal{L}(\mu \mid \tilde{\mathbf{x}}) &= \prod_{i=1}^{n} p_{\tilde{X}}(\tilde{x}_i \mid \mu) \\ &= \frac{\exp\left(-\frac{1}{\mu}\sum_{i=1}^{n} \tilde{x}_i\right)}{\mu^n (1 - e^{-t/\mu})^n} \end{aligned} \tag{5}$$

where $\tilde{\mathbf{x}} = [\tilde{x}_1, \ldots, \tilde{x}_n]'$, and $\{\tilde{x}_i\}_{i=1}^n$ is a size n sample of truncated SLI measurements. From the estimating equation, $\partial/\partial\mu \log \mathcal{L}(\mu|\tilde{\mathbf{x}}) = 0$, the ML estimator is derived as

$$\hat{\mu} = \frac{t}{e^{t/\hat{\mu}} - 1} + \frac{1}{n}\sum_{i=1}^{n} \tilde{x}_i. \tag{6}$$

This article has been accepted for inclusion in a future issue of this journal. Content is final as presented, with the exception of pagination.

This equation must be solved numerically. Note that $\hat{\mu}$ is equal to the sample mean (SM) estimator plus a correction term that accounts for the truncation. The specified false alarm rate P_{FA} can be related to the cdf, parameterized with the estimated mean value, as

$$P_{\mathrm{FA}} = 1 - P_X(T) = e^{-T/\hat{\mu}} \tag{7}$$

where T is the detection threshold that needs to be solved for.

2) MLI: From a set $\{X_i\}_{i=1}^{L}$ of independent and exponentially distributed SLI measurements with mean value μ, an L-look MLI value can be computed as

$$X_L = \frac{1}{L}\sum_{k=1}^{L} x_k. \tag{8}$$

The MLI variable follows a gamma distribution with order parameter L and a mean value μ [23]. Its pdf is

$$p_{X_L}(x) = \left(\frac{L}{\mu}\right)^{L} \frac{x^{L-1}e^{-Lx/\mu}}{\Gamma(L)} \tag{9}$$

where $\Gamma(a) = \int_0^\infty y^{a-1}e^{-y}dy$ is the gamma function, and its cdf is

$$P_{X_L}(x) = \frac{\gamma\left(L, \frac{Lx}{\mu}\right)}{\Gamma(L)} \tag{10}$$

with the lower incomplete gamma function $\gamma(a,b)$ defined as $\int_0^b y^{a-1}e^{-y}dy$. The pdf of $\tilde{X}_L$, the truncated MLI, becomes

$$p_{\tilde{X}_L}(x) = \begin{cases} \left(\frac{L}{\mu}\right)^{L} \frac{x^{L-1}e^{-xL/\mu}}{\gamma\left(L, \frac{tL}{\mu}\right)}, & 0 < x \le t \\ 0, & x > t. \end{cases} \tag{11}$$

In the SAR context, shape parameter L is replaced by the equivalent number of looks (ENL), which is a lowered version of L used pragmatically in the statistical modeling to account for correlation between the samples in $\{X_i\}_{i=1}^{L}$ [24]. The ENL can be estimated from the data and is considered an image constant. We can assume that it is known prior to the ship detection, and we are left with estimating the mean value μ.

An ML estimator for the mean can be also obtained from the likelihood function

$$\begin{aligned} \mathcal{L}(\mu \mid \tilde{\mathbf{x}}) &= \prod_{i=1}^{n} p_{\tilde{X}_L}(\tilde{x}_i \mid \mu) \\ &= \left(\frac{L}{\mu}\right)^{nL} \frac{e^{-\frac{L}{\mu}\sum_{i=1}^{n}\tilde{x}_i}}{\left[\gamma\left(L, \frac{tL}{\mu}\right)\right]^{n}} \prod_{i=1}^{n} \tilde{x}_i^{L-1} \end{aligned} \tag{12}$$

where $\{\tilde{x}_i\}_{i=1}^{n}$ is a size n sample of truncated MLI measurements. The log-likelihood function is derived as

$$\begin{aligned} \log \mathcal{L}(\mu \mid \tilde{\mathbf{x}}) = nL\log\frac{L}{\mu} - n\log\gamma\left(L, \frac{tL}{\mu}\right) \\ - \frac{nL}{\mu}\frac{1}{n}\sum_{i=1}^{n}\tilde{x}_i + n(L-1)\frac{1}{n}\sum_{i=1}^{n}\log(\tilde{x}_i) \end{aligned} \tag{13}$$

where $(1/n)\sum_{i=1}^{n}\tilde{x}_i$ and $(1/n)\sum_{i=1}^{n}\log(\tilde{x}_i)$ are SMs of the original and logarithmic truncated MLI measurements. Thus, the MLE estimate of the mean is

$$\hat{\mu} \subseteq \arg\max_{\mu}\left\{\log \mathcal{L}(\mu \mid \tilde{\mathbf{x}})\right\} \tag{14}$$

which must be solved numerically. The specified false alarm rate P_{FA} can be then related to the cdf with the estimated mean value as

$$P_{\mathrm{FA}} = 1 - P_{X_L}(T) = 1 - \frac{\gamma\left(L, \frac{LT}{\hat{\mu}}\right)}{\Gamma(L)} \tag{15}$$

where T is the detection threshold that needs to be solved for.

Since the exponential distribution is a special case of the gamma distribution, the results in Section II-B.1 are obtained from those in Section II-B.2 by setting $L = 1$.

C. Parameter Estimation Performance

All CFAR detectors rely upon accurate parameter estimation, which determines the goodness-of-fit of the hypothesized background clutter model. Both for SLI and MLI data, the mean value is the only parameter that must be estimated locally. The TS-based ML estimators are proposed in the previous section. This section provides empirical results that demonstrate how much loss the TS-based estimators experience due to the reduction of the estimation sample by truncation and how much the TS-based estimators gain compared with the conventional ML estimators designed for untruncated data when the estimation samples are contaminated.

Two parameters used in the experiments are first introduced to characterize the simulation of contaminated data and the operation of the TS-based estimators, respectively. Contamination ratio R_c is defined as the fraction of contaminated data points and the truncation ratio R_t as the fraction of truncated samples, both given relative to the total number of samples in the estimation window. The mean value estimators are examined with simulated exponential and gamma distributed sea clutter for two levels of statistical contamination: $R_c = 1\%$ and $R_c = 10\%$. The contamination samples are drawn from a uniform distribution whose support is 0.8 to 5 times the maximum value of the simulated sea clutter samples. Clutter samples are randomly replaced by the contaminated samples. The total sample size is held at $n = 1024$.

The estimator performances are demonstrated by analyzing the mean squared error (MSE), which is defined as

$$\begin{aligned} \mathrm{MSE}(\hat{\mu}) &= \mathrm{Var}(\hat{\mu}) + \mathrm{Bias}(\hat{\mu})^2 \\ &= E\left\{(\hat{\mu} - E\{\hat{\mu}\})^2\right\} + E\{\hat{\mu} - \mu\}^2 \\ &= E\left\{(\hat{\mu} - \mu)^2\right\}. \end{aligned} \tag{16}$$

Fig. 1 shows the MSE versus R_t for the exponential distribution estimator in panels (a) and (c) and for the gamma distribution estimator in panels (b) and (d). Panels (a) and (b) show the

This article has been accepted for inclusion in a future issue of this journal. Content is final as presented, with the exception of pagination.

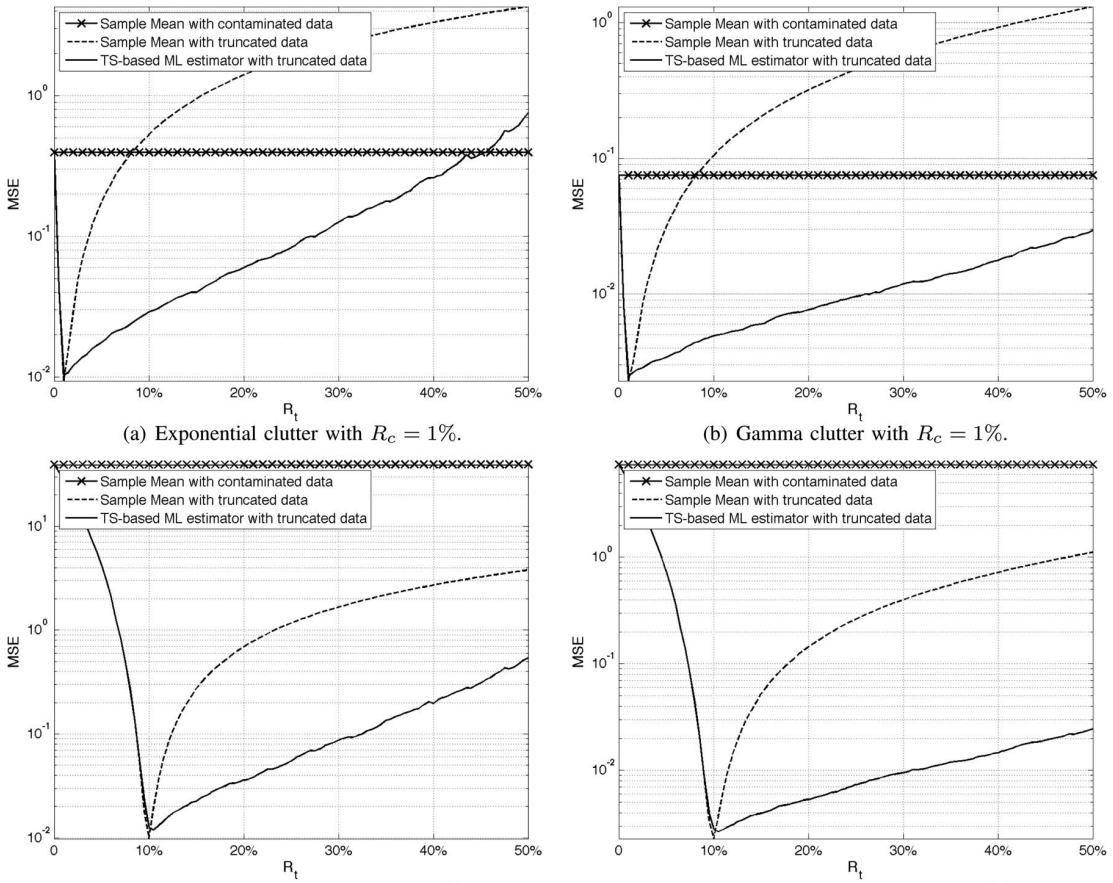

(a) Exponential clutter with $R_c = 1\%$.

(b) Gamma clutter with $R_c = 1\%$.

(c) Exponential clutter with $R_c = 10\%$.

(d) Gamma clutter with $R_c = 10\%$.

Fig. 1. Analysis of MSE versus R_t for three mean estimators: (i) SM estimator without truncation (solid lines with crosses); (ii) SM estimator with truncation (dashed lines); and (iii) TS-based ML estimators for truncated data (solid lines). Simulated sea clutter is drawn from an exponential distribution ($\mu = 3$) in (a) and (c) and from a gamma distribution ($\mu = 3$, $L = 4$) in (b) and (d). Contamination from a high-intensity uniform distribution is inserted with $R_c = 1\%$ in (a) and (b) and $R_c = 10\%$ in (c) and (d). The total sample size is held at $n = 1024$.

results for $R_c = 1\%$ and panels (c) and (d) for $R_c = 10\%$. Three estimators are compared in each plot.

i) The first is the ML estimator as derived for untruncated data, which is applied to the entire data sample, including contamination. This is equal to the SM estimator for both the exponential distribution and the gamma distribution.
ii) The second estimator is again the SM estimator, but it is now applied to truncated data, for which it is not ML nor theoretically justified in any other way.
iii) The third is our proposed TS-based ML estimators for the respective case. It is applied to truncated data, as it has been designed for.

Estimators (i) and (ii) are included in the comparison to exemplify the outcome of a nonrobust approach and a nonrigorous treatment of truncated data, respectively.

It can be observed throughout all the experiments that the SM estimator without truncation (solid lines with crosses) does not vary with R_t and produces a high constant MSE value since it does not offer any protection against contamination. The SM estimator with truncation (dashed lines) performs well when R_t matches R_c, but the performance rapidly gets worse as R_t grows since the truncation operation has not been accounted for in the derivation of the estimator. In practice, it is impossible to know in advance how many contaminated samples there are within each local estimation window. Therefore, it is difficult to select an R_t that matches R_c. The proposed estimators (solid lines) perform much better than the SM estimator with truncation as R_t grows beyond R_c. Even in the extreme case, when R_t goes up to 50%, the TS-based ML estimators are still able to provide reasonable outcomes. The increase in MSE with R_t is naturally a result of the estimation sample becoming smaller and smaller. Still, the number of data points that must be truncated before the MSE exceeds the level of the SM estimator without truncation is not likely to be reached in practical applications. Thus, the proposed estimators produce convincing results.

In summary, despite an inevitable increase in MSE due to the sample size reduction for the proposed TS-based ML estimators, the alternative estimators suffer more performance degradations due to contamination or nonrigorous handling of the truncated data. The gain of appropriately compensating for

This article has been accepted for inclusion in a future issue of this journal. Content is final as presented, with the exception of pagination.

the truncation operation is such that the proposed estimators outperform the alternatives for all practically relevant truncation depths. Note that the estimators' performance rapidly deteriorates when R_t drops below R_c, which emphasizes the contamination damage to the parameter estimation and the need to choose a safe R_t value.

III. CFAR Detector Characteristics

In this section, two important CFAR detector characteristics are investigated, i.e., the false alarm regulation property and the ROC, with both simulated exponentially distributed SLI clutter and gamma distributed MLI clutter. The proposed TS-CFAR detector is compared with the conventional CA-CFAR and OS-CFAR detectors, whose IC schemes are also considered and discussed.

A. Definitions of Characteristics

1) False Alarm Regulation Property: The observed false alarm rate is defined as

$$P_{\mathrm{fa}} = \frac{n_{\mathrm{fa}}}{n} \tag{17}$$

where n_{fa} and n are the number of false alarms and the total number of samples, respectively. Compliance of the specified false alarm rate P_{FA} and the observed false alarm rate P_{fa} is an indicator of the sea clutter modeling accuracy, but it also depends on the accuracy in the estimation of model parameters. A constant P_{fa} can be approached if the hypothesized statistical background model and the associated parameter estimates are accurate. This is a fundamental property that justifies the CFAR label. Nevertheless, a pragmatic solution is often used when a detection algorithm does not satisfy the false alarm regulation property: A P_{FA} is chosen that produces a P_{fa} that meets the practical requirements, although the two do not match. In operational systems, P_{FA} is set according to, e.g., the image resolution and end application. In practice, P_{FA} is commonly set to around 0.001% (or 10^{-5}) for fine-resolution SAR images.

2) ROC: The detection rate is measured as

$$P_d = \frac{n_d}{n_t} \tag{18}$$

where n_d and n_t are the number of correctly detected targets and the total number of target samples, respectively. To investigate detection performance, the P_d measurements are usually evaluated at different values of P_{FA}. P_d monotonically increases with P_{FA}, and a plot of these two properties against each other is commonly referred to as an ROC curve. It characterizes the tradeoff between P_d and P_{FA} for a given CFAR detector and is used to compare detector performance. P_d is sometimes plotted against P_{fa} instead of P_{FA}. This makes sense when the false alarm regulation property is not satisfied since P_{fa} represents actual performance whereas P_{FA} is merely a design parameter.

B. Experiments With Monte Carlo Simulations

In this paper, experiments are based on simulated SLI and MLI measurements of sea clutter drawn from the exponential distribution ($\mu = 3$) and the gamma distribution ($\mu = 3$, $L = 4$), respectively. Random data points in these background samples are replaced by new values representing the contamination by nonoceanic targets. Like in Section II-C, the contamination samples are uniformly distributed in the range of 0.8 to 5 times the maximum value of the sea clutter data. The contamination ratios considered are $R_c = \{1\%, 5\%, 10\%, \text{ and } 20\%\}$.

Monte Carlo simulations are conducted, where each simulation represents one reference window with a sample size of 1024 and certain amount of contaminations defined by R_c. Note that the simulated contaminated pixels also represent the potential target pixels in each reference window. All tested CFAR detectors are applied in each simulated reference window, where the falsely detected clutter pixels and the correctly detected contaminated pixels are counted. Finally, all those numbers of falsely and correctly detected pixels are added together and then divided by the total number of simulated samples calculated from the product of the total number of simulations and the sample size of each simulated reference window. Therefore, the observed false alarm rate P_{fa} and the detection rate P_d can be derived as

$$P_{\mathrm{fa}} = \frac{\sum_1^m \{n_{\mathrm{fa}}\}_i}{m \times n_{\mathrm{win}}}$$

$$P_d = \frac{\sum_1^m \{n_d\}_i}{m \times n_{\mathrm{win}} \times R_c}$$

where m is the total number of simulations, n_{win} is the number of samples of each reference window, and $\{n_{\mathrm{fa}}\}_i$ and $\{n_d\}_i$ are the number of falsely detected clutter pixels (false alarms) and the number of correctly detected contaminated pixels (potential targets) in each reference window, respectively. In order to reach the minimum specified false alarm rate level, $P_{\mathrm{FA}} = 10^{-6}$, at least $m = 5 \times 10^6$ simulations are conducted for all tested situations.

C. Compared CFAR Algorithms

Before conducting experiments with simulated exponentially distributed SLI clutter and gamma distributed MLI clutter, we introduce the algorithms to be compared. The TS-CFAR detector was presented in Section II. The remaining detectors, i.e., CA-CFAR, ICCA-CFAR, OS-CFAR, and ICOS-CFAR, are briefly described in the following.

1) CA-CFAR Detector: This is the simplest detector available, where an estimate of the mean clutter intensity is produced by averaging a set of samples surrounding the cell under test [15]. The conventional algorithm assumes that the background sample is homogeneous and contains no interfering targets. Thus, the CA-CFAR offers no protection against target interference, but it is still used extensively in operational systems.

2) ICCA-CFAR Detector: An IC scheme was proposed by Barboy *et al.* [10], and similar versions were repeated in [13] and [14], where iteratively updated outlier maps are used for

This article has been accepted for inclusion in a future issue of this journal. Content is final as presented, with the exception of pagination.

censoring. The IC scheme is specifically aimed at dense target environments, and the algorithm is robust even in situations where targets and associated artifacts take up 30% of the reference window [10]. One weakness of the IC approach is that the censoring may remove sea clutter data and targets, thus removing data in the upper tail of the sea clutter distribution. This is not accounted for in the parameter estimators, and the detection threshold is consequently underestimated, although this effect may be alleviated during iterations. Hence, the detection procedure may need a number of "spike rejection" iterations, which requires long computation time. The IC process has converged when the outlier map is stable. In the experiments, we have set an upper limit of 30 iterations to avoid an excessive number of iterations. The IC scheme can be combined with any CFAR detector, and the ICCA-CFAR detector is the specific implementation of the IC principle with the CA-CFAR detector.

3) OS-CFAR Detector: The OS-CFAR trades a small loss in detection performance under homogeneous background conditions, relative to the CA-CFAR detector, for an improved performance under less ideal background scenarios. In practice, the method is performed by rank-ordering the values encountered in the neighborhood area according to their increasing magnitude and by selecting a certain predefined value from the ordered sequence [9]. This can be the median, the minimum, the maximum, or any other value. Thus, this procedure excludes the reference samples with larger magnitudes, which may contain contaminating targets, and estimates the background statistics from the remaining samples [18]. Such signal processing methods are denoted as methods with an ordered statistic.

The central idea of an OS-CFAR procedure is to select one certain value $X_{(k)}$, $k \in \{1, 2, \ldots, N\}$ from the rank-ordered ascending sequence and to use it as a representation $Z = X_{(k)}$ of the clutter power level as observed in the reference window. Since $X_{(k)}$ is the kth value of the ordered statistic for the random variables $X_1, \ldots, X_N$, its pdf can be derived as [25]

$$p_{X_{(k)}}(x) = k \binom{N}{k} \left[1 - P_X(x)\right]^{N-k} \left[P_X(x)\right]^{k-1} p_X(x) \quad (19)$$

where $p_X(x)$ is the pdf and $P_X(x)$ is the cdf of the random variables in the reference window. The specified false alarm ratio P_{FA} indicates the probability that the value Y_0 of the cell under test is mistakenly interpreted as a target during the threshold decision, and it is given as

$$\begin{aligned} P_{\mathrm{FA}} &= P[Y_0 \geq KZ] \\ &= \int_0^\infty \left(1 - P_X(Kx)\right)\, p_{X_{(k)}}(x)\, dx \end{aligned} \quad (20)$$

where K is a scaling factor. Both pdfs of Y_0 and Z need to be known. When the random variables $Y_0, X_1, \ldots, X_N$ of the clutter are assumed to follow an exponential distribution, P_{FA} can be computed from [9]

$$P_{\mathrm{FA}} = k \binom{N}{k} \frac{(k-1)!(K+N-k)!}{(K+N)!}. \quad (21)$$

When a gamma distributed clutter is assumed, P_{FA} is derived as

$$P_{\mathrm{FA}} = k \binom{N}{k} \int_0^\infty \left(1 - \frac{\gamma(L, Ky)}{\Gamma(L)}\right) \left(1 - \frac{\gamma(L, y)}{\Gamma(L)}\right)^{N-k} \times \left(\frac{\gamma(L, y)}{\Gamma(L)}\right)^{k-1} \frac{y^{L-1} e^{-y}}{\Gamma(L)}\, dy \quad (22)$$

where shape parameter L is replaced again by known image constant ENL, and K needs to be solved numerically. Note that the scaling factor K, which controls the false alarm probability P_{FA}, does not depend on the average clutter power μ of the exponentially or gamma distributed parent population. Thus, they may be considered as CFAR methods. In the following paragraphs, they are denoted by the term OS-CFAR. As suggested in a previous study [9], we choose k equal $3N/4$.

4) ICOS-CFAR Detector: As for CA-CFAR, the IC scheme can be also applied to the OS-CFAR detector, and its realization is, in the following paragraphs, referred to as the ICOS-CFAR detector.

D. Experimental Results

This section compares all algorithms listed above, but not in the same figure. If all detectors were compared simultaneously, the wide range spanned by their performance measures and the overlap of the many curves would make it difficult to discern and interpret the details of the experiments. Instead, we first compare the CA-CFAR detector with the ICCA-CFAR detector, then the OS-CFAR detector with the ICOS-CFAR detector, before presenting results for the TS-CFAR detector alone. We finally compare the best performing algorithms, i.e., the ICCA-CFAR, the ICOS-CFAR, and the TS-CFAR detectors.

1) CA-CFAR and ICCA-CFAR Detectors: Fig. 2 presents an analysis of the false alarm regulation property and ROC curves for the CA-CFAR and the ICCA-CFAR detectors.

Fig. 2(a) and (b) shows the ratio of P_{fa} to P_{FA} in decibels against P_{FA}. When $P_{\mathrm{fa}}/P_{\mathrm{FA}}$ goes to zero on the logarithmic scale, P_{fa} approaches P_{FA}, as desired. Note that no value is plotted when there are no observed false alarms, i.e., the logarithm of the ratio goes to minus infinity. It is clear that ICCA-CFAR, as compared with CA-CFAR, has an observed false alarm rate closer to the specified false alarm rate P_{FA}. As expected, we also notice that an increase in the contamination ratio R_c points toward a larger deviation from P_{FA}. Fig. 2(c) and (d) presents the detection rate versus the specified false alarm rate, and it is clear that the ICCA-CFAR detector is much superior to the CA-CFAR detector at the same contamination levels. Especially for CA-CFAR, it is also evident that a larger R_c decreases the detection rate.

2) OS-CFAR and ICOS-CFAR Detectors: Fig. 3 presents an analysis of the false alarm regulation property and ROC curves for the OS-CFAR and ICOS-CFAR detectors.

Fig. 3(a) and (b) shows that the ICOS-CFAR detector has very good false alarm regulation properties. It confirms what was observed in Fig. 2, i.e., that the IC approach is very robust with respect to contamination within the reference window. Fig. 3(c) and (d) presents the detection rate versus the specified

This article has been accepted for inclusion in a future issue of this journal. Content is final as presented, with the exception of pagination.

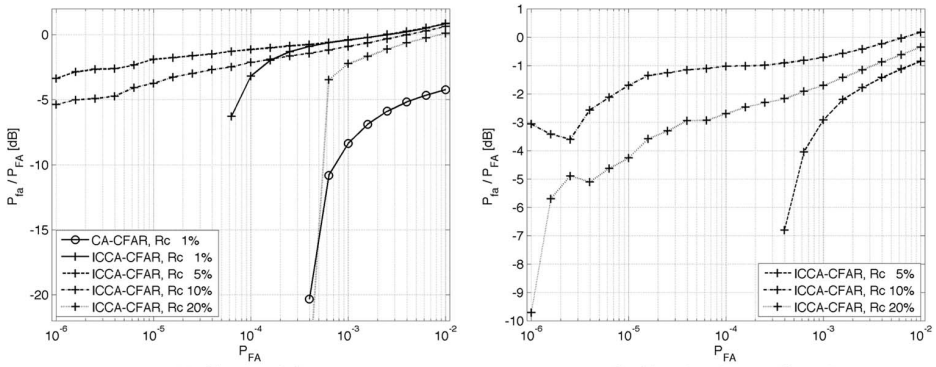

(a) Simulated SLI. (b) Simulated MLI ($L = 4$).

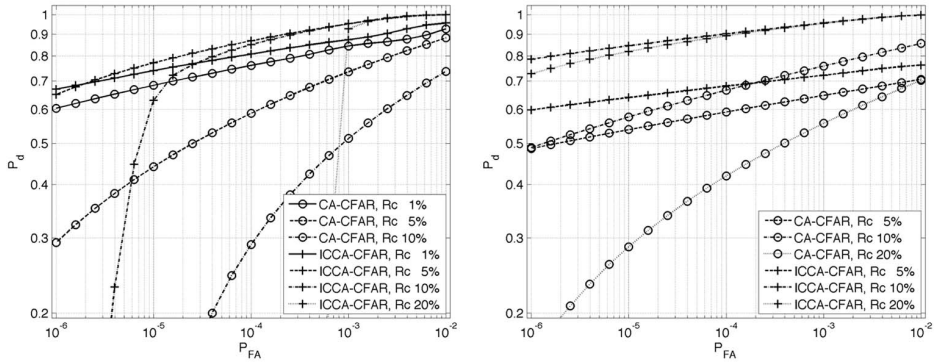

(c) Simulated SLI. (d) Simulated MLI ($L = 4$).

Fig. 2. False alarm regulation property and ROC analysis for CA- and ICCA-CFAR in (a), (b) and (c), (d). Simulated SLI and MLI sea clutter are applied with exponential ($\mu = 3$) and gamma ($\mu = 3, L = 4$) distributions, respectively. The contamination ratios considered are 1%, 5%, and 10%, related to the total number of reference samples. A log scale is applied on the x-axes in all subfigures and y-axes in (c) and (d).

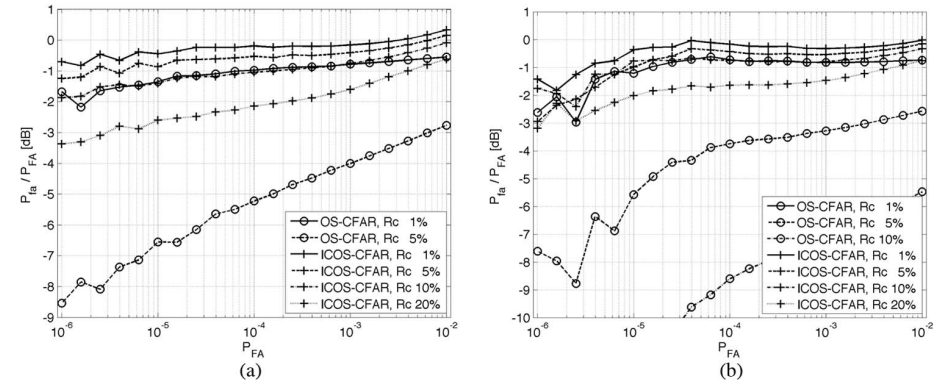

(a) (b)

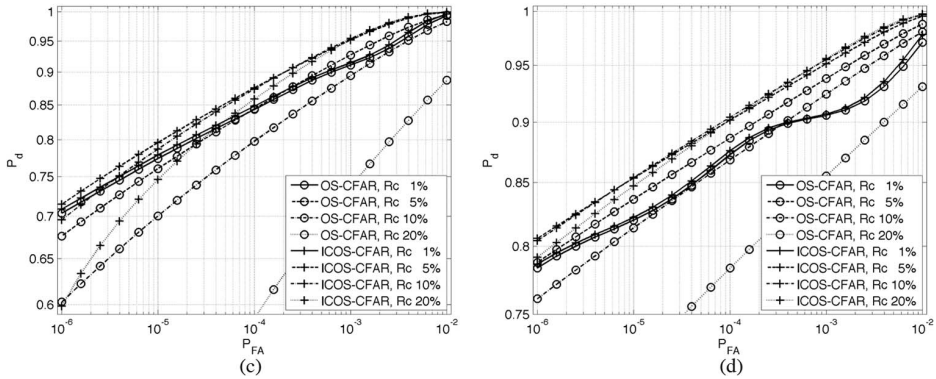

(c) (d)

Fig. 3. False alarm regulation property and ROC analysis for OS- and ICOS-CFAR in (a), (b) and (c), (d). Simulated SLI and MLI sea clutter are applied with exponential ($\mu = 3$) and gamma ($\mu = 3, L = 4$) distributions, respectively. The contamination ratios considered are 1%, 5%, and 10%, related to the total number of reference samples. A log scale is applied on the x-axes in all subfigures and y-axes in (c) and (d). (a) Simulated SLI. (b) Simulated MLI ($L = 4$). (c) Simulated SLI. (d) Simulated MLI ($L = 4$).

This article has been accepted for inclusion in a future issue of this journal. Content is final as presented, with the exception of pagination.

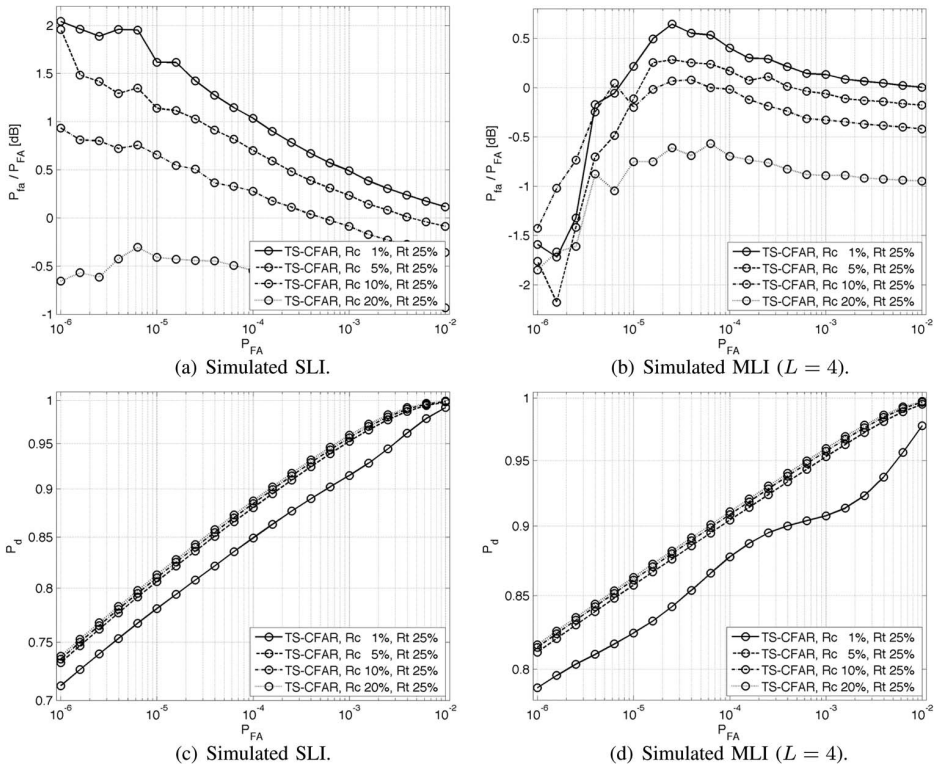

(a) Simulated SLI. (b) Simulated MLI ($L = 4$).

(c) Simulated SLI. (d) Simulated MLI ($L = 4$).

Fig. 4. False alarm regulation property and ROC analysis for TS-CFAR in (a), (b) and (c), (d). Simulated SLI and MLI sea clutter are applied with exponential ($\mu = 3$) and gamma ($\mu = 3$, $L = 4$) distributions, respectively. The contamination ratios considered are 1%, 5%, and 10%, related to the total number of reference samples. A log scale is applied on the x-axes in all subfigures and y-axes in (c) and (d).

false alarm rate, and again, we see that the IC scheme improves the result. Our investigation shows that the OS-based detectors are able to produce reasonably good results even when the contamination ratio approaches 20%, which is not the case for the CA-based detectors.

3) TS-CFAR Detector: Fig. 4 presents an analysis of the false alarm regulation property and ROC curves for the TS-CFAR detector, which was introduced in Section II.

To demonstrate the robustness of the proposed TS-based algorithm, we fix $R_t = 25\%$ while varying R_c. In general, the TS-CFAR detector shows consistent behavior and good performance. An interesting observation is that it achieves higher detection rate P_d as R_c increases, which should be explained: The high R_t ensures that all target pixels are removed from the estimation sample, regardless of R_c. The truncated samples thus consist of a constant number of sea clutter measurements, but their distribution and upper bound will vary with R_c. When R_c is low, many pixels from the sea clutter distribution will be truncated and the truncation depth t obtains a low value. As R_c rises, more target pixels and less sea clutter pixels are truncated, and thus t becomes higher. The ROC curves clearly show that a high t value is preferred to a lower value of t. This conclusion would be further strengthened if we evaluated P_d versus the observed P_{fa} instead of the specified P_{FA}.

4) Comparative Analysis: The IC versions of the CA- and OS-CFAR algorithms show superior performance as compared with their conventional detector schemes. Therefore, for concise comparison, the proposed TS-CFAR detector here is only compared with the ICCA-CFAR and ICOS-CFAR detectors. Figs. 5–8 present the comparative analysis of the false alarm regulation property and ROC curves for different contamination conditions. Note that the truncation ratio of the TS-CFAR detector is still set to 25% for all tested cases, which has similarities to the OS-based algorithm when $k = 3N/4$ (see Section III-C.3).

The ICCA-CFAR detector shows a large deviation from P_{FA} and a quick drop in detection rate as a function of increasing contamination ratio. The ICOS algorithm shows a certain degree of improvement over the ICCA algorithm. However, as the contamination ratio gets larger, it is obvious that the TS algorithm still obtains an observed false alarm rate closer to the specified values and an improved stable detection rate.

So far, two classic CFAR detector performance measures (characteristics) have been discussed in this section with different specified false alarm rates (P_{FA}), ranging from 10^{-6} to 10^{-2}. In practice, false alarm rates equal to or smaller than 10^{-5} are usually applied. Next, we fix $P_{\mathrm{FA}} = 10^{-5}$ and present detailed plots of P_d versus P_{fa}. The experiments are also conducted through Monte Carlo simulations.

Tables I and II present the CFAR detector characteristics analysis with the specified false alarm rate at $P_{\mathrm{FA}} = 10^{-5}$. Results are averaged from 1000 Monte Carlo simulations with a sample size of 1024. The contamination ratios considered are 1%, 5%, 10%, and 20%, related to the total number of reference samples. The truncation ratio of the TS-CFAR detector is constant at $R_t = 25\%$. The best results are emphasized in boldface.

This article has been accepted for inclusion in a future issue of this journal. Content is final as presented, with the exception of pagination.

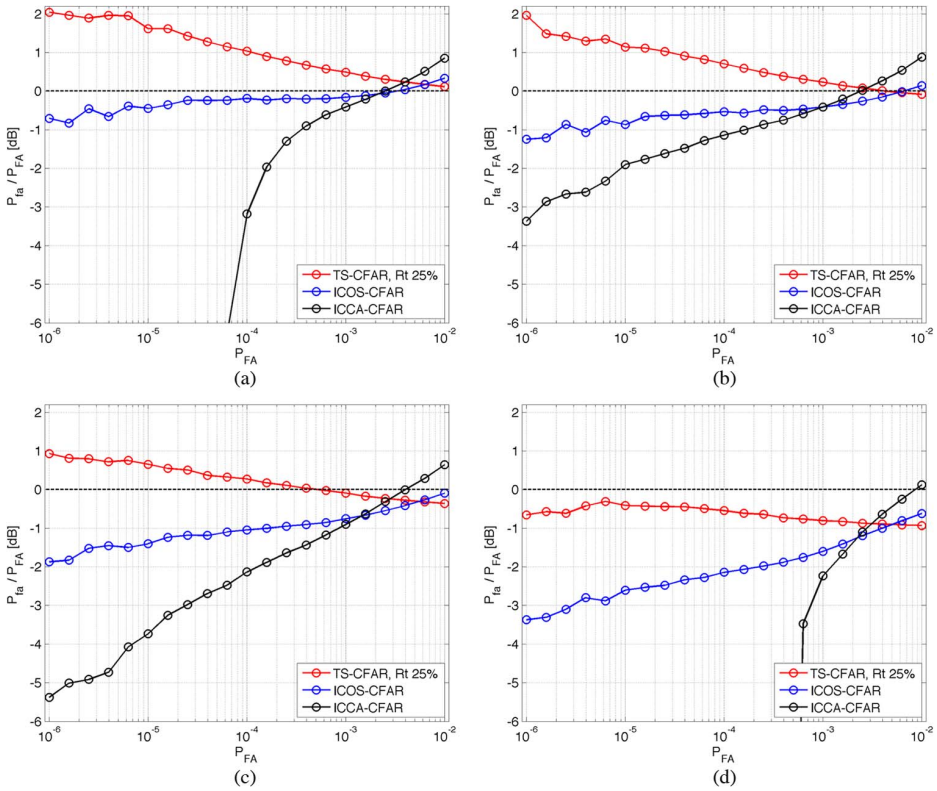

Fig. 5. Comparative analysis of the false alarm regulation property of the best performing detectors. Simulated SLI sea clutter is applied with exponential distribution ($\mu = 3$). The contamination ratios considered are 1%, 5%, 10%, and 20%, related to the total number of reference samples. A log scale is applied on the x-axes. (a) $R_c = 1\%$. (b) $R_c = 5\%$. (c) $R_c = 10\%$. (d) $R_c = 20\%$.

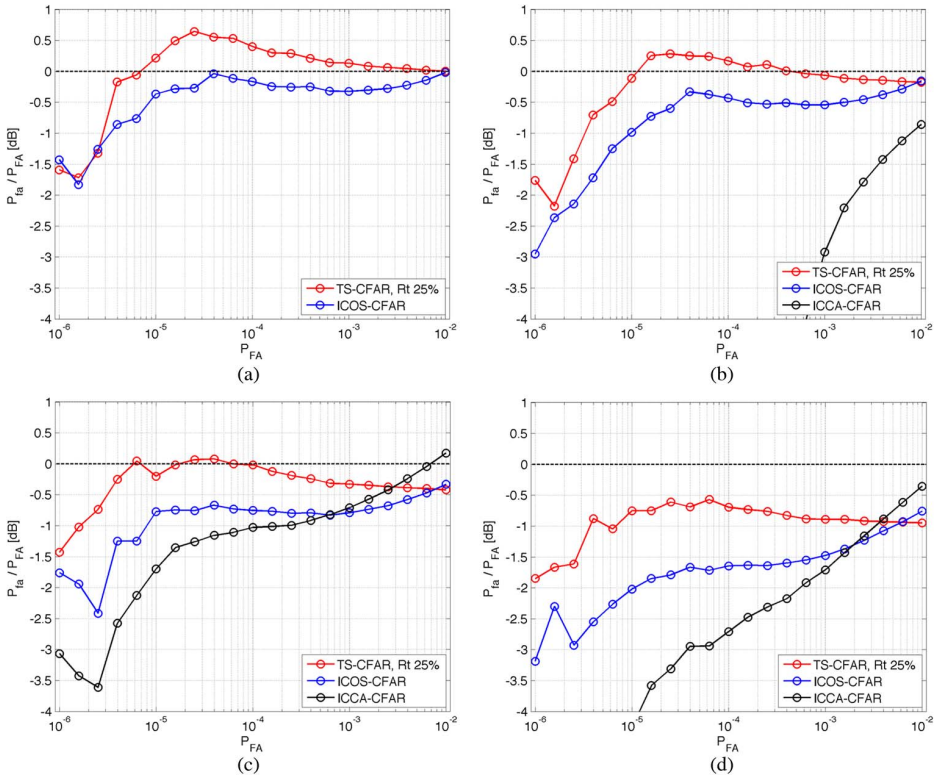

Fig. 6. Comparative analysis of the false alarm regulation property of the best performing detectors. Simulated MLI sea clutter is applied with gamma distribution ($\mu = 3, L = 4$). The contamination ratios considered are 1%, 5%, 10%, and 20%, related to the total number of reference samples. A log scale is applied on the x-axes. (a) $R_c = 1\%$. (b) $R_c = 5\%$. (c) $R_c = 10\%$. (d) $R_c = 20\%$.

This article has been accepted for inclusion in a future issue of this journal. Content is final as presented, with the exception of pagination.

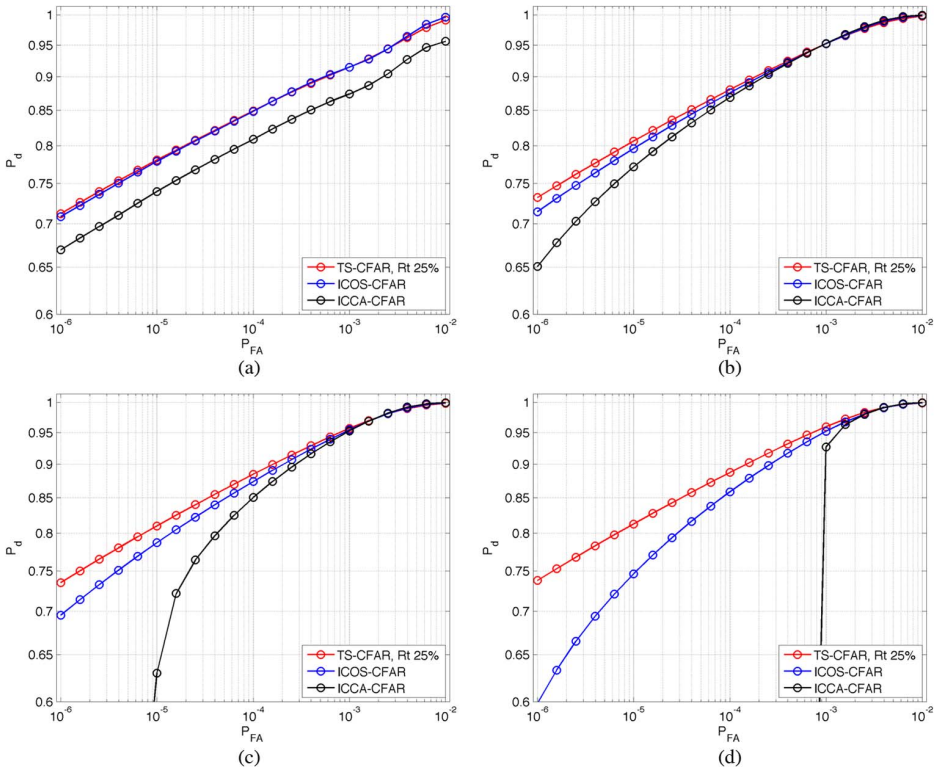

Fig. 7. Comparative analysis of ROC of the best performing detectors. Simulated SLI sea clutter is applied with exponential distribution ($\mu = 3$). The contamination ratios considered are 1%, 5%, 10%, and 20%, related to the total number of reference samples. A log scale is applied on the x-axes and y-axes. (a) $R_c = 1\%$. (b) $R_c = 5\%$. (c) $R_c = 10\%$. (d) $R_c = 20\%$.

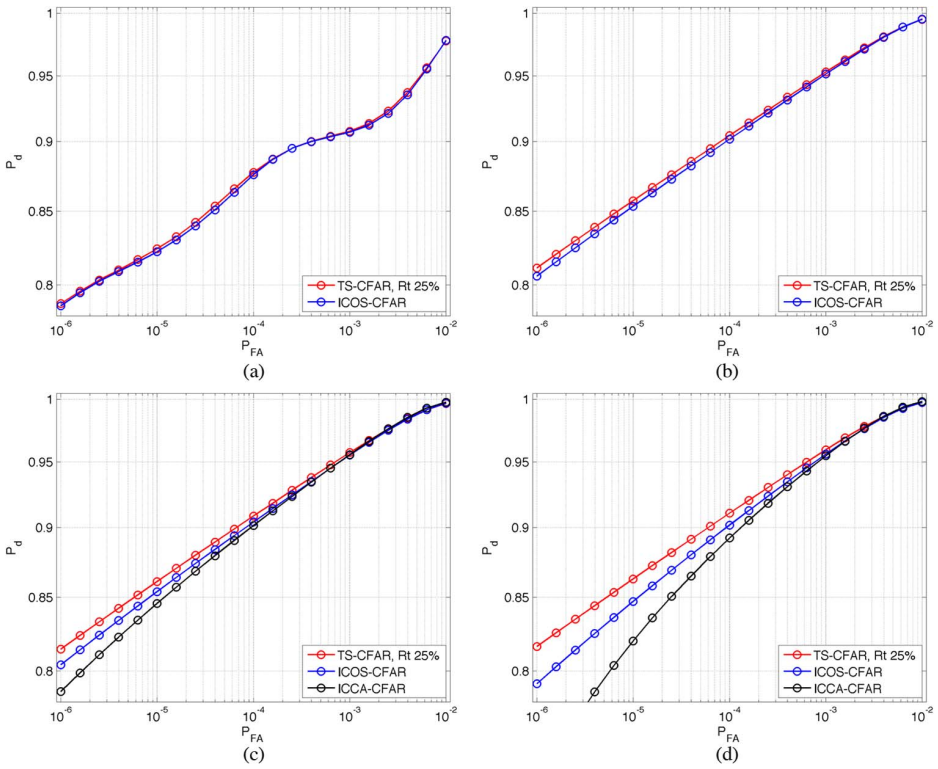

Fig. 8. Comparative analysis of ROC of the best performing detectors. Simulated MLI sea clutter is applied with gamma distribution ($\mu = 3, L = 4$). The contamination ratios considered are 1%, 5%, 10%, and 20%, related to the total number of reference samples. A log scale is applied on the x-axes and y-axes. (a) $R_c = 1\%$. (b) $R_c = 5\%$. (c) $R_c = 10\%$. (d) $R_c = 20\%$.

This article has been accepted for inclusion in a future issue of this journal. Content is final as presented, with the exception of pagination.

TABLE I
CFAR DETECTOR CHARACTERISTICS ANALYSIS WITH THE SPECIFIED FALSE ALARM RATE AT $P_{\mathrm{FA}} = 10^{-5}$. SIMULATED SLI SEA CLUTTER IS APPLIED WITH EXPONENTIAL DISTRIBUTION ($\mu = 3$). RESULTS ARE AVERAGED FROM 1000 MONTE CARLO SIMULATIONS WITH A SAMPLE SIZE OF 1024. THE CONTAMINATION RATIOS CONSIDERED ARE 1%, 5%, 10%, AND 20%, RELATED TO THE TOTAL NUMBER OF REFERENCE SAMPLES. THE TRUNCATION RATIO OF THE TS-CFAR DETECTOR IS CONSTANT AT $R_t = 25\%$. THE BEST RESULTS ARE SHOWN IN BOLDFACE

	P_{fa}/P_{FA} [dB]					P_d [%]				
	CA	ICCA	OS	ICOS	TS	CA	ICCA	OS	ICOS	TS
$R_c = 1\%$	$-\infty$	$-\infty$	-1.4148	**-0.5298**	1.4791	68.40	73.99	77.37	77.84	**78.03**
$R_c = 5\%$	$-\infty$	-2.0150	-6.5093	**-0.8589**	1.0895	44.01	77.11	76.02	79.58	**80.59**
$R_c = 10\%$	$-\infty$	-3.6033	-15.3463	-1.4016	**0.5628**	6.80	63.00	70.00	78.68	**80.97**
$R_c = 20\%$	$-\infty$	$-\infty$	$-\infty$	-2.7248	**-0.5524**	0	0	43.34	74.62	**81.25**

TABLE II
CFAR DETECTOR CHARACTERISTICS ANALYSIS WITH THE SPECIFIED FALSE ALARM RATE AT $P_{\mathrm{FA}} = 10^{-5}$. SIMULATED MLI SEA CLUTTER IS APPLIED WITH GAMMA DISTRIBUTION ($\mu = 3, L = 4$). RESULTS ARE AVERAGED FROM 1000 MONTE CARLO SIMULATIONS WITH A SAMPLE SIZE OF 1024. THE CONTAMINATION RATIOS CONSIDERED ARE 1%, 5%, 10%, AND 20%, RELATED TO THE TOTAL NUMBER OF REFERENCE SAMPLES. THE TRUNCATION RATIO OF THE TS-CFAR DETECTOR IS CONSTANT AT $R_t = 25\%$. THE BEST RESULTS ARE SHOWN IN BOLDFACE

	P_{fa}/P_{FA} [dB]					P_d [%]				
	CA	ICCA	OS	ICOS	TS	CA	ICCA	OS	ICOS	TS
$R_c = 1\%$	$-\infty$	$-\infty$	-1.0261	-0.3642	**0.3469**	0.05	0.05	81.95	82.16	**82.35**
$R_c = 5\%$	$-\infty$	$-\infty$	-4.6803	-0.6623	**0.1138**	54.07	64.26	83.60	85.28	**85.68**
$R_c = 10\%$	$-\infty$	-1.7213	-10.5455	-1.0009	**-0.1576**	57.54	84.51	81.34	85.33	**86.04**
$R_c = 20\%$	$-\infty$	-3.9493	-32.2187	-1.9547	**-0.7791**	28.59	81.93	71.35	84.65	**86.23**

Note that some ratio values go to minus infinity, which means that no false alarms are found.

For a fair comparison of detection rates P_d, they should all correspond to the same observed false alarm rate P_{fa}. However, the P_d values are computed based on a specified false alarm rate P_{FA} since it is impractical to control P_{fa}, which is a stochastic variable that depends on the data sample. The approach we have taken in Tables I and II is to list P_d values (computed for $P_{\mathrm{FA}} = 10^{-5}$) and $10\log_{10}(P_{\mathrm{fa}}/P_{\mathrm{FA}})$ values separately and use the latter in the interpretation of the P_d values.

In the joint analysis of $P_d(P_{\mathrm{FA}})$ versus $P_{\mathrm{fa}}/P_{\mathrm{FA}}$, a value of $10\log_{10}(P_{\mathrm{fa}}/P_{\mathrm{FA}}) > 0$ signifies that the corresponding value of P_d is higher than it would have been if P_{fa} was equal to the specified P_{FA}, as desired. Therefore, $P_d(P_{\mathrm{FA}})$ overestimates the performance of the algorithm. Conversely, a value of $10\log_{10}(P_{\mathrm{fa}}/P_{\mathrm{FA}}) < 0$ means that the corresponding $P_d(P_{\mathrm{FA}})$ underestimates the algorithm performance. This knowledge can be used to compensate for the inadequacy of $P_d(P_{\mathrm{FA}})$, although the resulting analysis is only qualitative.

This leads to the following interpretations: Table I shows that TS-CFAR produces the highest values of $P_{\mathrm{fa}}/P_{\mathrm{FA}}$ and also obtains the highest $P_d(P_{\mathrm{FA}})$ in the exponential case. According to the joint analysis described above, the TS-CFAR detection rates are therefore exaggerated, whereas the detection rates of the other algorithms are underrated. Similarly, we see in Table II that TS-CFAR has the highest P_d also in the gamma case. Again, the $P_{\mathrm{fa}}/P_{\mathrm{FA}}$ values show that the comparison unfairly favors the TS-CFAR algorithm and indicates that the internal ranking of the algorithms based on the desired $P_d(P_{\mathrm{fa}})$ might be different than what we obtain from the listed $P_d(P_{\mathrm{FA}})$.

In Figs. 9 and 10, we plot P_d versus P_{fa}, as desired, but with an artifact: The P_d values are produced with simulated data samples that are generated according to a specified P_{FA} value. Since the data samples are random, so are the P_{fa} and P_d values they produce. This is reflected in Figs. 9 and 10, where a colored cloud of (P_{fa}, P_d) points represents the stochastic performance measures obtained at $P_{\mathrm{FA}} = 10^{-5}$ for the different algorithms. The number of false alarms in a random generated data sample is known from (17) as $n_{\mathrm{fa}} = P_{\mathrm{fa}} \cdot n$. The discrete nature of the point clouds at low P_{FA} levels reflects that the realizations of n_{fa} are small integers, which give rise to the observed discrete levels. We see again in these figures that the TS-CFAR algorithm produces the highest P_d, but if all results were projected to a common P_{fa} level, their P_d levels would also change in an unknown manner, and thus, the internal ranking of the algorithms is not obvious in all cases.

What we can conclude is that the TS-CFAR algorithm performs at least on par with the ICOS-CFAR algorithm, which we consider as state of the art for the multiple-target situation. The conventional CA-CFAR detector performs poorly with contaminated samples, as expected. It is worth noting that the OS-based CFAR detectors show relatively good detection rates. However, their observed false alarm rates deviate much from the specified false alarm rate, particularly when operating without the IC scheme. Overall, the proposed TS-CFAR detector shows the best false alarm regulation properties and obtains excellent detection rates without resorting to the IC strategy, which is inevitably associated with high computational cost.

IV. DETECTION PERFORMANCE WITH COMPOSITE REAL DATA

In this section, a comparative study of the CFAR detectors based on example cases is presented. In all cases studied, the sea clutter statistics are occasionally contaminated by pixels originating from targets. A proper treatment of the difficulties that may rise due to clutter edges and transitions in sea state is left out here and kept for future work. All experiments and examples discussed are carefully constructed; hence, the background sea clutter is kept homogeneous without any nonstationary

This article has been accepted for inclusion in a future issue of this journal. Content is final as presented, with the exception of pagination.

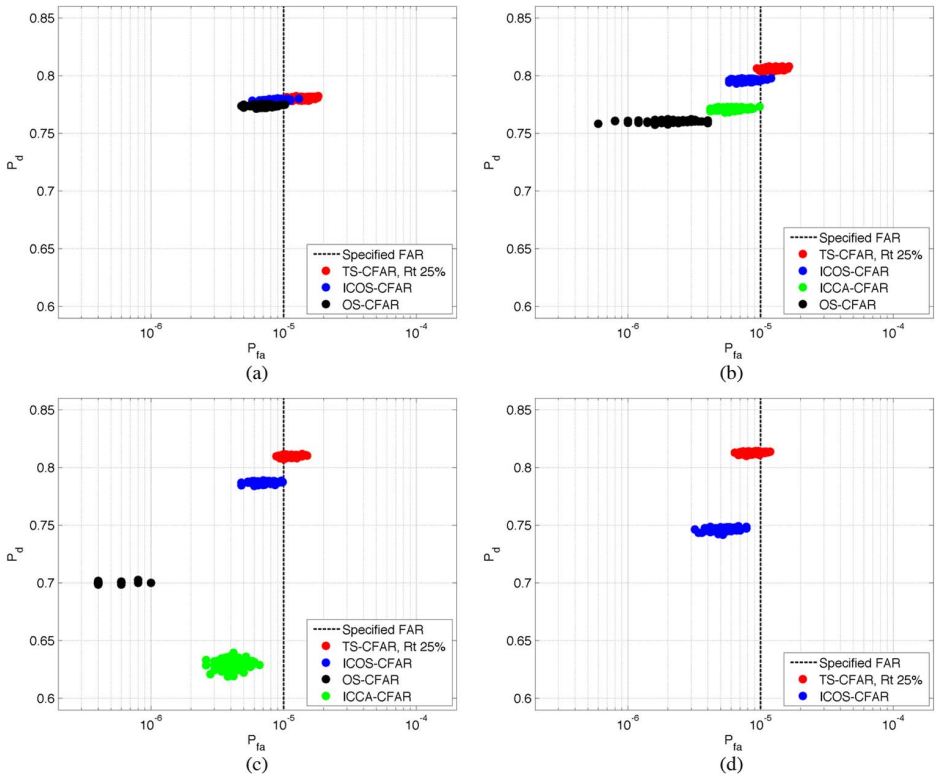

Fig. 9. ROC-type plot of observed false alarm rate against detection rate at specified false alarm rate $P_{\mathrm{FA}} = 10^{-5}$. Simulated SLI sea clutter is applied with exponential distributed ($\mu = 3$). Monte Carlo simulations are done with a sample size of 1024. Each data cloud is based on 1000 repetitions. Note that, over the selected range of contamination conditions, not all color clouds are visible due to the chosen intervals on the axes. (a) $R_c = 1\%$. (b) $R_c = 5\%$. (c) $R_c = 10\%$. (d) $R_c = 20\%$.

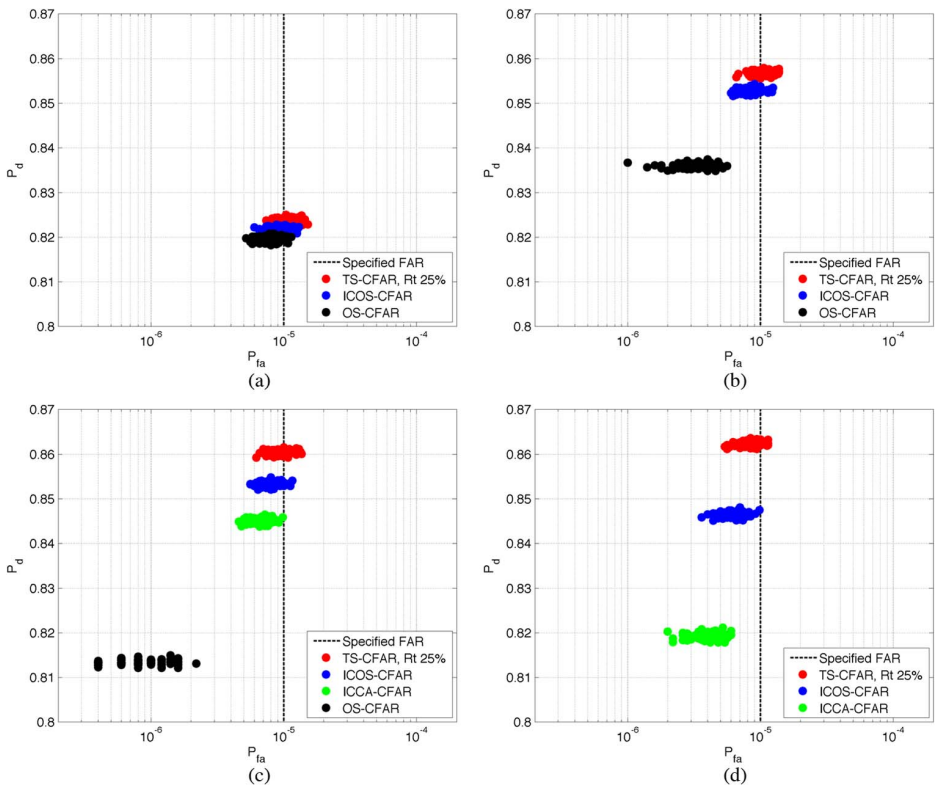

Fig. 10. ROC-type plot of observed false alarm rate against detection rate at specified false alarm rate $P_{\mathrm{FA}} = 10^{-5}$. Simulated MLI sea clutter is applied with gamma distribution ($\mu = 3, L = 4$). Monte Carlo simulations are done with a sample size of 1024. Each data cloud is based on 1000 repetitions. Note that, over the selected range of contamination conditions, not all color clouds are visible due to the chosen intervals on the axes. (a) $R_c = 1\%$. (b) $R_c = 5\%$. (c) $R_c = 10\%$. (d) $R_c = 20\%$.

This article has been accepted for inclusion in a future issue of this journal. Content is final as presented, with the exception of pagination.

statistics before we superimpose targets. The proposed TS-CFAR detector is compared with the conventional CA-CFAR and OS-CFAR detectors and their IC schemes. Note that the TS, OS, and IC schemes are all proposed to handle multiple-target situations. The performances of the CFAR detectors are investigated and discussed from three practical perspectives, namely, the impact of adjusting the design of the sliding window, the detectors' behavior in dense target situations, and the target blurring and merging effect due to multilooking.

The truncation ratio of the TS-CFAR detector is kept constant at $R_t = 25\%$ to allow fair comparison with the OS-based algorithm at $k = 3N/4$. It is worth noting that the reference sample size applied under the sliding window technique directly affects the parameter estimation of the hypothesized model and, hence, the statistical analysis of the background clutter. More samples generally lead to more accurate estimates and an improved model fit. However, more samples require larger reference sliding windows, which increases the risk of including both contamination and nonstationary statistics, e.g., outliers and clutter edges. A relatively large reference sample size is implemented in our experiments, with a total number of samples set to 1024 before data truncation, and a specified false alarm rate of $P_{\mathrm{FA}} = 10^{-5}$ is set throughout the performance evaluation of the CFAR detectors for all example cases.

A Radarsat-2 SLC fine quad-polarization SAR imagery acquired on August 18, 2011, off the south coast of the U.K. at Portsmouth Harbor is exploited to evaluate the detectors. The resolution of the imagery is approximately 5.0 and 4.7 m along the azimuth and range directions, respectively. The scene is acquired with a mid-swath incidence angle of approximately 38°, and the test area is characterized by low wind conditions and a calm-sea state [26]. Portsmouth is one of the most crowded harbors in the U.K., which provides a good test opportunity for a wide range of vessel sizes and vessel types, including several small boats under 10 m in length. The ground truth is based on Automatic Information System positioning data and photographic evidence [26]. Three example cases are composited from the HV polarization SLI and MLI ($L = 4$) SAR measurements and utilized in the proceeding experiments. Note that we perform multilooking in the spatial domain with a resolution-preserving sliding window, and not with a stepping window, which is the common practice. This has no impact on the analysis and the results we obtain, except that it provides more data that can be used in the evaluation of the algorithms, and is therefore considered a valid approach.

A. Sliding Window Design

The sliding window technique is commonly applied in CFAR detection schemes. When the central cell under test contains a strong target, sidelobe effects may contaminate the background sample in both the azimuth and range directions. A common and pragmatic solution to this problem is to define a guard area and confine the selection of background data to the four corners of the sliding window. A schematic of this approach is given in Fig. 11(a). An alternative method is shown in Fig. 11(b), where a block estimation window centered at the cell under test is chosen.

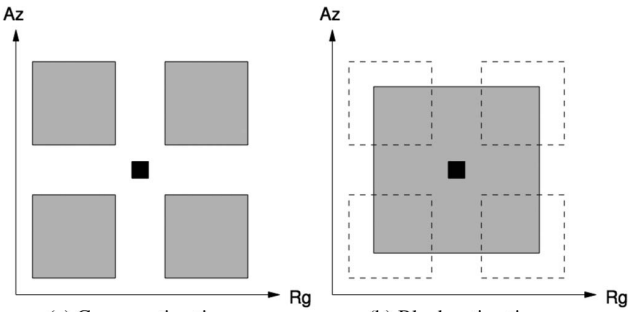

(a) Corner estimation. (b) Block estimation.

Fig. 11. Alternative ways of selecting the estimation window for sea clutter statistics. The cell under test is marked in black, and the estimation sample is shaded. In the study, four 16×16 windows in (a) and a 32×32 window in (b) are applied.

The choice of sliding window design naturally affects the detection results of CFAR detectors. In our implementation of the design illustrated in Fig. 11(b), a 32×32 window is applied to provide a total of 1024 reference samples before we exclude the central test cell. For the corner approach, 16×16 samples are drawn from each of the four corners, providing the same total number of reference samples.

Both block and corner sliding window designs are investigated here. A comparative analysis of the CFAR detectors is shown in Figs. 12 and 13. The composited SLI and MLI scenes contain one target. The IC schemes take approximately nine iterations to reach convergence on average.

In general, with the corner approach, bright pixels originating from the target are excluded from the background clutter sample, which leads to more accurate parameter estimation and more beneficial thresholding. In the composite case shown in Figs. 12(a) and 13(a), excessive energy from the target gives a blurred impression along the azimuth direction due to the sidelobe effect. Note that both pixels originating from the vessel and its smeared-out energy are treated here as target pixels. In Figs. 12(b) and (c) and 13(b) and (c), it is clear that CA-based CFAR detectors relay on a proper design of sliding window for various background clutter conditions, which is due to a lack of accommodating contaminating targets in the sea clutter estimation window. The OS-based CFAR detectors in Figs. 12(d) and (e) and 13(d) and (e) offer some improvements in this regard, and we note that the corner estimation approach yields superior results. As shown in Figs. 12(f) and 13(f), it is obvious that the proposed TS-CFAR detector produces the best detection results without additional iterative processing and has a robust performance regarding the choice of estimation window approach. Hence, reference window designs incorporating guard areas are made superfluous, as the TS-CFAR detector can be readily implemented based on the block approach, thus collecting the reference samples from a more confined area centered at the cell under test.

B. Interfering Targets

Target suppression in CFAR detection is an adverse effect due to densely located targets. When a target lies within the reference window of the target under test, the resulting overestimated

This article has been accepted for inclusion in a future issue of this journal. Content is final as presented, with the exception of pagination.

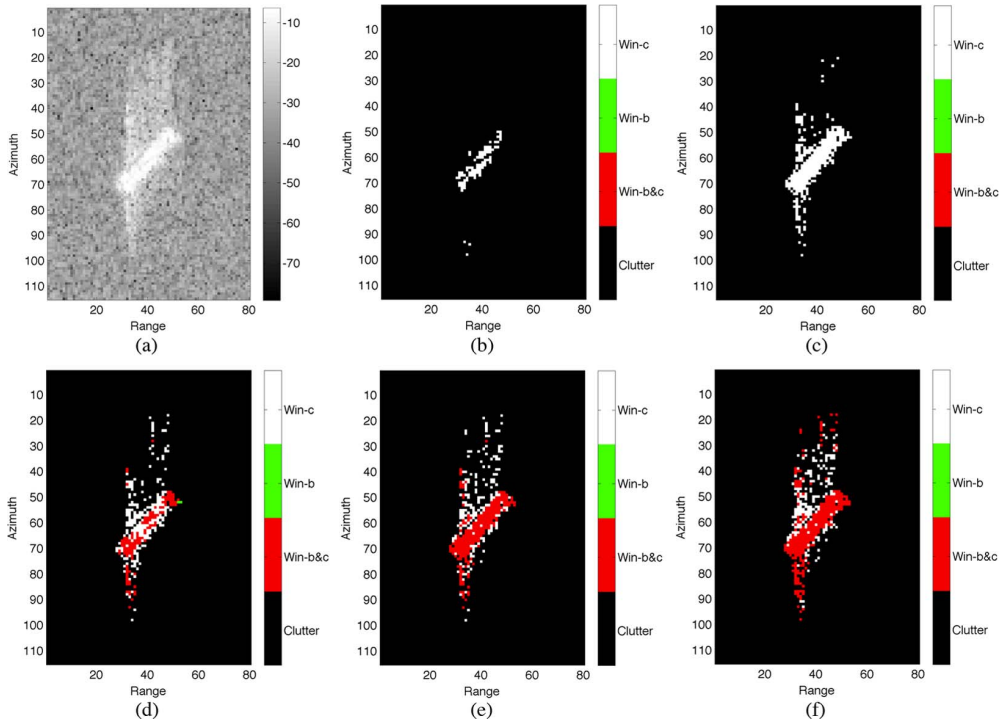

Fig. 12. Comparative analysis of detection results with block and corner sliding windows. Composite SLI HV polarization SAR image is applied with the specified false alarm rate at $P_{\mathrm{FA}} = 0.001\%$. The color bar in (b)–(f) represents detected targets using the corner estimation approach (Win-c, white), the block estimation approach (Win-b, green), and the combined results from both approaches (Win-b&c, red). Black represents pixels detected as background clutter by the respective CFAR detector. (a) Composite SLI SAR image in decibels. (b) CA-CFAR detection results. (c) ICCA-CFAR detection results. (d) OS-CFAR detection results. (e) ICOS-CFAR detection results. (f) TS-CFAR detection results ($R_t = 25\%$).

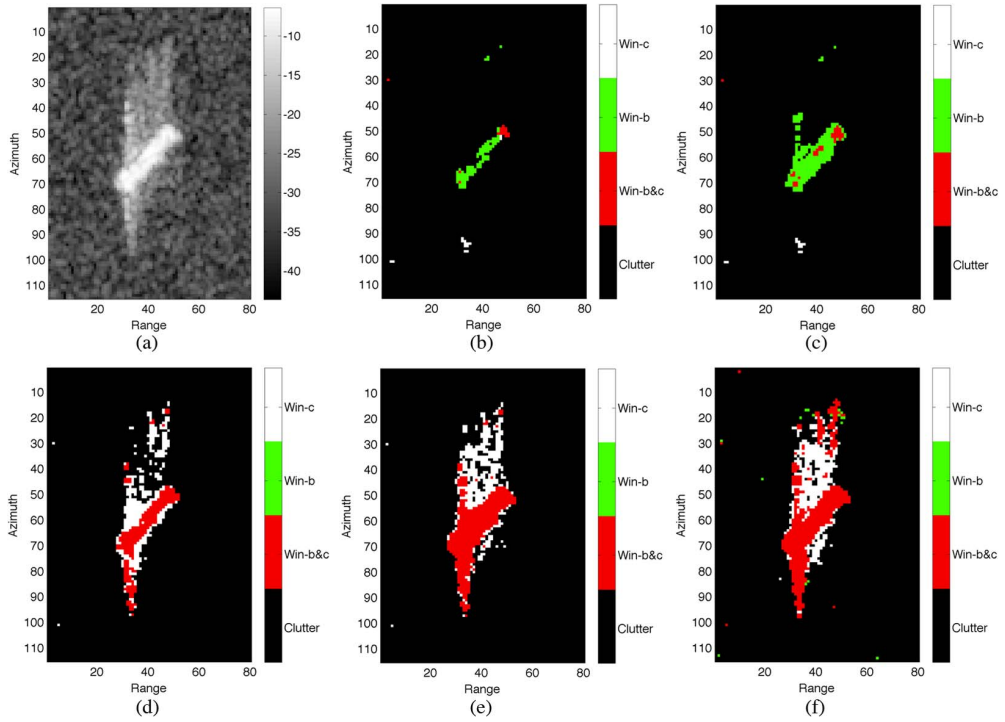

Fig. 13. Comparative analysis of detection results with block and corner sliding windows. Composite MLI HV polarization SAR image with number of looks $L = 4$ is applied with the specified false alarm rate at $P_{\mathrm{FA}} = 0.001\%$. The color bar in (b)–(f) represents detected targets using the corner estimation approach (Win-c, white), the block estimation approach (Win-b, green), and the combined results from both approaches (Win-b&c, red). Black represents pixels detected as background clutter by the respective CFAR detector. (a) Composite MLI SAR image in decibels. (b) CA-CFAR detection results. (c) ICCA-CFAR detection results. (d) OS-CFAR detection results. (e) ICOS-CFAR detection results. (f) TS-CFAR detection results ($R_t = 25\%$).

This article has been accepted for inclusion in a future issue of this journal. Content is final as presented, with the exception of pagination.

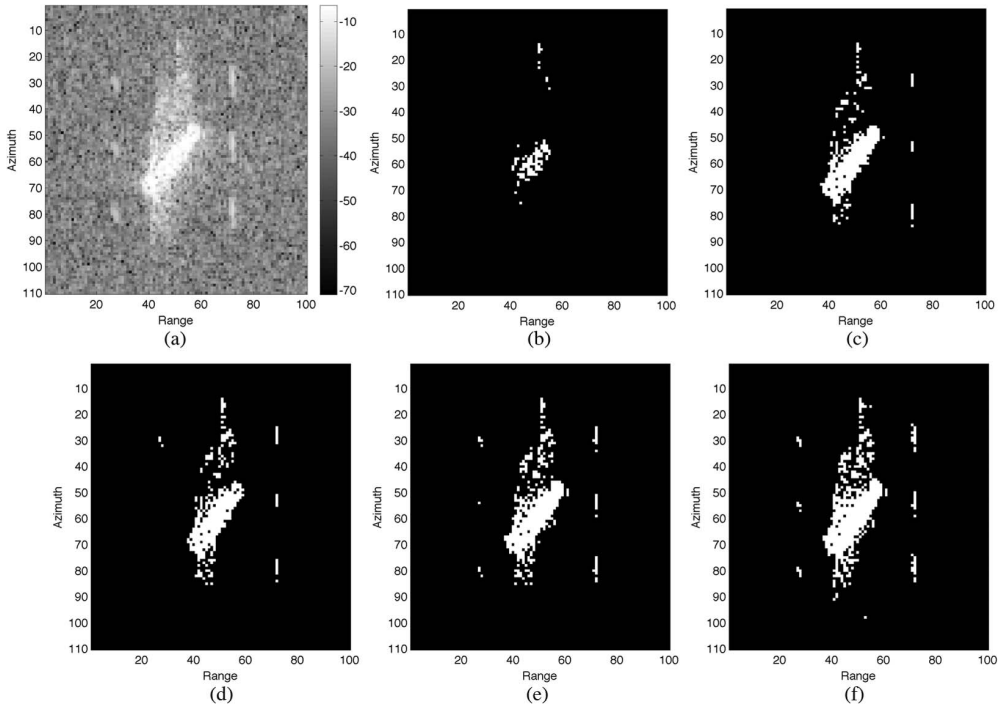

Fig. 14. Comparative analysis of detection results with multiple interfering targets. Composite SLI HV polarization SAR image is applied with the specified false alarm rate at $P_{\mathrm{FA}} = 0.001\%$. The composite example SAR scene contains one large vessel and six small targets. The corner approach for estimating sea clutter statistics is applied in (b)–(f). (a) Composite SLI SAR image in decibels. (b) CA-CFAR detection results. (c) ICCA-CFAR detection results. (d) OS-CFAR detection results. (e) ICOS-CFAR detection results. (f) TS-CFAR detection results ($R_t = 25\%$).

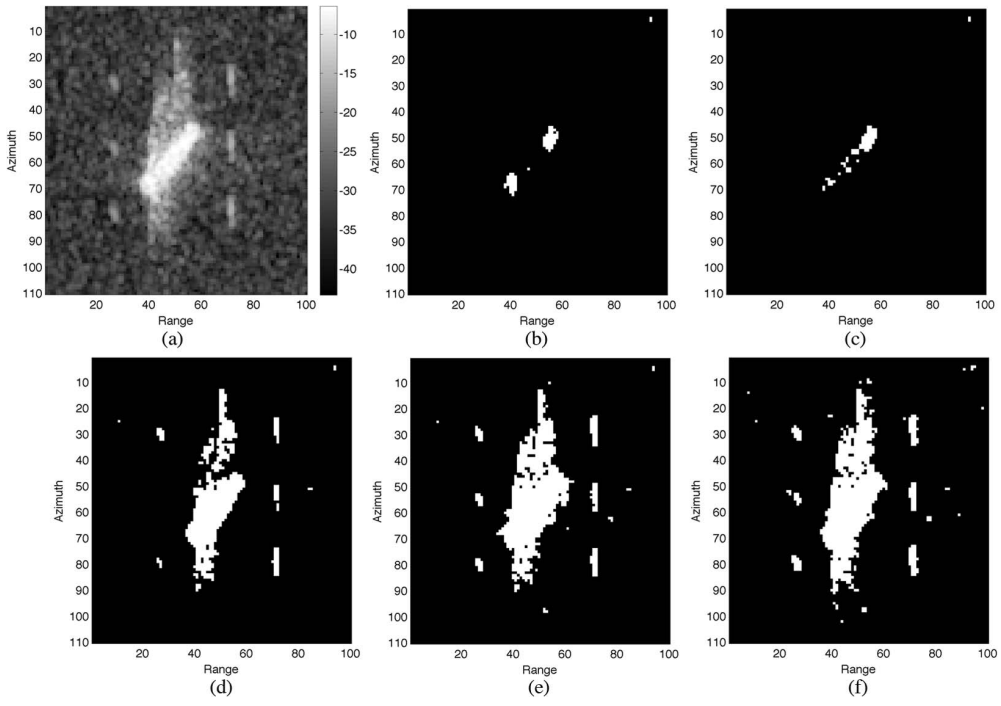

Fig. 15. Comparative analysis of detection results with multiple interfering targets. Composite MLI HV polarization SAR image with number of looks $L = 4$ is applied with the specified false alarm rate at $P_{\mathrm{FA}} = 0.001\%$. The composite example SAR scene contains one large vessel and six small targets. The corner approach for estimating sea clutter statistics is applied in (b)–(f). (a) Composite MLI SAR image in decibels. (b) CA-CFAR detection results. (c) ICCA-CFAR detection results. (d) OS-CFAR detection results. (e) ICOS-CFAR detection results. (f) TS-CFAR detection results ($R_t = 25\%$).

threshold can cause the target under test to not be detected [1]. In Figs. 14 and 15, the performances of the different detectors are compared through an example case, where a large vessel is placed in the center with six small targets lining up on both sides. Note that all six interfering targets are real targets composited from other parts of the same source SAR imagery. The corner approach for sampling sea clutter pixels is applied for all detectors compared.

This article has been accepted for inclusion in a future issue of this journal. Content is final as presented, with the exception of pagination.

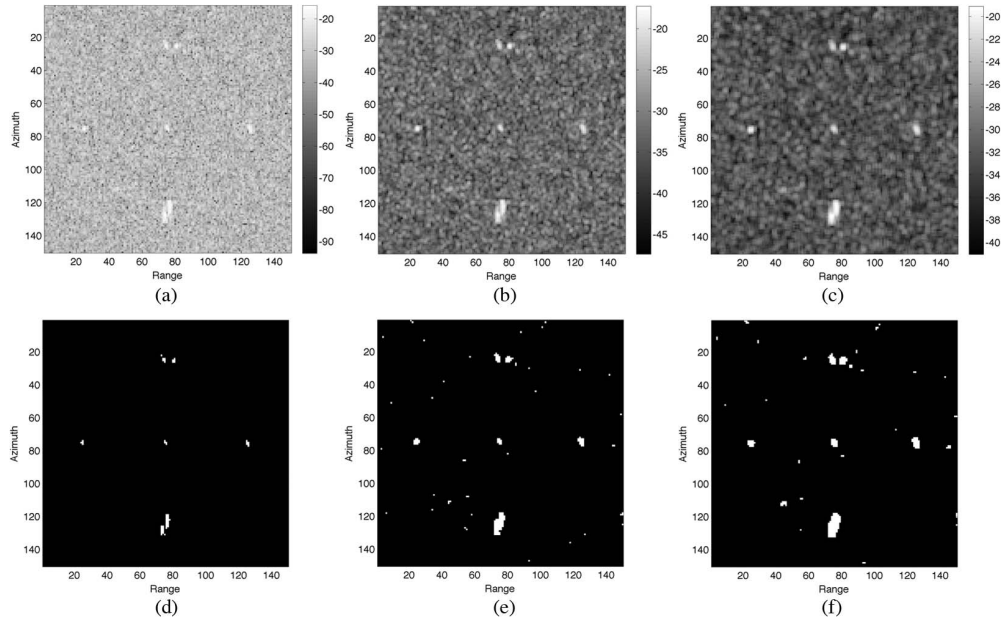

Fig. 16. Comparative analysis of TS-CFAR detection results with multiple small closely located targets. First row (a)–(c): composite example HV polarization SAR data; one SLI and two MLI images with varying number of looks L. The legends are in decibels. Note that two small targets are placed close together in the upper central part of the scene, and three small targets are placed on the line in the middle, whereas the target located in the lower central part of the image is likely to be composed of two vessels. Second row (d)–(f): TS-CFAR detection results on corresponding SLI or MLI images from the first row. The corner approach for estimating sea clutter statistics is applied. The specified false alarm rate is 0.001%, and the truncation ratio is fixed at 25%.

In Figs. 14(b) and 15(b), the CA-CFAR detector performs poorly, causing a significant number of undetected target pixels. The ICCA-CFAR detector in Fig. 14(c) completely misses the three small targets on the left side of the panel after 10 iterations, and in Fig. 15(c), it performs even worse with the applied corner sliding window after 12 iterations. It is obvious from a visual inspection of the results in Figs. 14(f) and 15(f) that the TS-CFAR detector performs best. The TS-CFAR detector detects pixels from all targets, as does the ICOS-CFAR detector after seven and six iterations in Figs. 14(e) and 15(e), respectively. However, the TS-CFAR detector is superior in the total number of target pixels detected.

C. Blurring and Merging Targets

So far, the proposed TS-CFAR detector shows robust and outstanding detection results. In addition, we demonstrate how the TS-CFAR detector behaves with different multilooked SAR images. A composite example, including small and closely separated targets, is used in this experiment. As we know, multilooking is often applied in SAR image processing for speckle reduction. However, the inevitable blurring effect cannot be neglected, particularly when aiming at detecting small targets with weak contrast. In MLI data, when two targets are closely located, the detections from both targets are likely to be merged. It is worth noting that the process of multilooking averages the correlated measurements in real SAR images, which affects statistical modeling of the resulting multilooked data.

Fig. 16(a)–(c) shows composite example SAR intensity images with number of looks $L = 1, 4$, and 9, respectively. It is clear that the image becomes blurred with an increasing number of looks. The TS-CFAR detector performance is then examined with fixed truncation ratio $R_t = 25\%$ and specified false alarm rate $P_{\mathrm{FA}} = 0.001\%$. For the SLI image, the TS-CFAR detector is sensitive enough to detect and distinguish all small and closely located targets, as shown in Fig. 16(d). With the increasing number of looks in Fig. 16(e) and (f), all detected targets get blurred as expected; meanwhile, closely located targets are merged.

V. Conclusion

In order to reduce the bias of the estimated background statistics in multiple-target situations, the TS-CFAR detector has been proposed. The TS-CFAR algorithm is based on TSs and has a number of advantages. It is designed to accommodate interfering targets in the reference window. False alarms are also controlled exceptionally well by the TS-CFAR algorithm. The comparisons of the different CFAR detectors have clearly demonstrated the superiority of TS-CFAR processing over conventional CA-CFAR and OS-CFAR processing. TS-CFAR also performs on par with IC schemes while avoiding the iterations.

In practical CA-CFAR applications, guard cells are used for separating the cell under test from the reference area in order to prevent target returns from falsifying the clutter level estimation. In TS-CFAR processing, guard cells become unnecessary since a small number of target amplitudes occurring within the reference area have almost no influence on the clutter level estimation. Due to the truncation, the TS-CFAR algorithm can be implemented with a block sliding estimation window centered at the cell under test, thus collecting the sample in a more confined area. Therefore, a reference window without guard cells can be used with TS-CFAR processing.

The TS-CFAR scheme is derived here for exponential and gamma distributed sea clutter background models with respect to SLI and MLI SAR measurements. In the future, potential expansions of the proposed algorithm could be made by deriving the TS-CFAR detector for other choices of hypothesized sea clutter models such as the common K-distribution.

This article has been accepted for inclusion in a future issue of this journal. Content is final as presented, with the exception of pagination.

ACKNOWLEDGMENT

The authors would like to thank Dr. A. P. Doulgeris and T. Kræmer at the University of Tromsø-The Arctic University of Norway for valuable discussions. They would also like to specially thank Dr. A. Marino at the Institute of Environmental Engineering, ETH Zürich, for sharing valuable Radarsat-2 SAR data sets from Portsmouth, U.K.

RADARSAT-2 Data and Products © MacDonald, Dettwiler and Associates Ltd. (2010)—All Rights Reserved. RADARSAT is an official mark of the Canadian Space Agency.

REFERENCES

[1] G. Trunk, "Range resolution of targets using automatic detectors," *IEEE Trans. Aerosp. Electron. Syst.*, vol. AES-14, no. 5, pp. 750–755, Sep. 1978.

[2] V. Hansen and J. Sawyers, "Detectability loss due to "Greatest Of" selection in a cell-averaging CFAR," *IEEE Trans. Aerosp. Electron. Syst.*, vol. AES-16, no. 1, pp. 115–118, Jan. 1980.

[3] M. Smith and P. Varshney, "Intelligent CFAR processor based on data variability," *IEEE Trans. Aerosp. Electron. Syst.*, vol. 36, no. 3, pp. 837–847, Jul. 2000.

[4] P. McLane, P. Wittke, and C. K.-S. Ip, "Threshold control for automatic detection in radar systems," *IEEE Trans. Aerosp. Electron. Syst.*, vol. AES-18, no. 2, pp. 242–248, Mar. 1982.

[5] E. Al-Hussaini and B. Ibrahim, "Comparison of adaptive cell-averaging detectors for multiple-target situations," in *Proc. Inst. Elect. Eng.—F Commun., Radar Signal Process.*, vol. 133, no. 3, pp. 217–223, Jun. 1986.

[6] M. Barkat, S. Himonas, and P. Varshney, "CFAR detection for multiple target situations," *Proc. Inst. Elect. Eng.—F Radar Signal Process.*, vol. 136, no. 5, pp. 193–209, Oct. 1989.

[7] S. Himonas and M. Barkat, "Automatic censored CFAR detection for nonhomogeneous environments," *IEEE Trans. Aerosp. Electron. Syst.*, vol. 28, no. 1, pp. 286–304, Jan. 1992.

[8] J. Rickard and G. Dillard, "Adaptive detection algorithms for multiple-target situations," *IEEE Trans. Aerosp. Electron. Syst.*, vol. AES-13, no. 4, pp. 338–343, Jul. 1977.

[9] H. Rohling, "Radar CFAR thresholding in clutter and multiple target situations," *IEEE Trans. Aerosp. Electron. Syst.*, vol. AES-19, no. 4, pp. 608–621, Jul. 1983.

[10] B. Barboy, A. Lomes, and E. Perkalski, "Cell-averaging CFAR for multiple-target situations," *Proc. Inst. Elect. Eng.—F Commun., Radar Signal Process.*, vol. 133, no. 2, pp. 176–186, Apr. 1986.

[11] P. Gandhi and S. Kassam, "Analysis of CFAR processors in homogeneous background," *IEEE Trans. Aerosp. Electron. Syst.*, vol. 24, no. 4, pp. 427–445, Jul. 1988.

[12] A. Farrouki and M. Barkat, "Automatic censoring CFAR detector based on ordered data variability for nonhomogeneous environments," *Proc. Inst. Elect. Eng.—Radar, Sonar Navigat.*, vol. 152, no. 1, pp. 43–51, Feb. 2005.

[13] G. Gao, L. Liu, L. Zhao, G. Shi, and G. Kuang, "An adaptive and fast CFAR algorithm based on automatic censoring for target detection in high-resolution SAR images," *IEEE Geosci. Remote Sens. Lett.*, vol. 47, no. 6, pp. 1685–1697, Jun. 2009.

[14] Y. Cui, G. Zhou, J. Yang, and Y. Yamaguchi, "On the iterative censoring for target detection in SAR images," *IEEE Geosci. Remote Sens. Lett.*, vol. 8, no. 4, pp. 641–645, Jul. 2011.

[15] H. M. Finn and R. S. Johnson, "Adaptive detection mode with threshold control as a function of spatially sampled clutter-level estimates," *RCA Rev.*, vol. 29, pp. 414–464, Sep. 1968.

[16] S. Blake, "OS-CFAR theory for multiple targets and nonuniform clutter," *IEEE Trans. Aerosp. Electron. Syst.*, vol. 24, no. 6, pp. 785–790, Nov. 1988.

[17] S. Himonas, "Adaptive censored greatest-of CFAR detection," in *Proc. Inst. Elect. Eng.—Radar Signal Process.*, vol. 139, no. 3, pp. 247–255, Jun. 1992.

[18] M. El Mashade, "Monopulse detection analysis of the trimmed mean CFAR processor in nonhomogeneous situations," *Proc. Inst. Elect. Eng.—Radar, Sonar Navigat.*, vol. 143, no. 2, pp. 87–94, Apr. 1996.

[19] J. Ritcey, "Performance analysis of the censored mean-level detector," *IEEE Trans. Aerosp. Electron. Syst.*, vol. AES-22, no. 4, pp. 443–454, Jul. 1986.

[20] E. Conte, M. Lops, and A. Tulino, "Hybrid procedure for CFAR in non-Gaussian clutter," *Proc. Inst. Elect. Eng.—Radar, Sonar Navigat.*, vol. 144, no. 6, pp. 361–369, Dec. 1997.

[21] E. Magraner, N. Bertaux, and P. Refregier, "Detection in gamma-distributed nonhomogeneous backgrounds," *IEEE Trans. Aerosp. Electron. Syst.*, vol. 46, no. 3, pp. 1127–1139, Jul. 2010.

[22] N. Balakrishnan and A. Basu, *The Exponential Distribution: Theory, Methods and Applications*. New York, NY, USA: Gordon and Breach, 1995.

[23] C. Oliver and S. Quegan, *Understanding Synthetic Aperture Radar Images*, ser. SciTech Radar and Defense Series. Raleigh, NC, USA: SciTech Publ., 2004.

[24] S. Anfinsen, A. Doulgeris, and T. Eltoft, "Estimation of the equivalent number of looks in polarimetric synthetic aperture radar imagery," *IEEE Trans. Geosci. Remote Sens.*, vol. 47, no. 11, pp. 3795–3809, Nov. 2009.

[25] H. Büning and G. Trenkle, *Nichtparametrische Statistische Methoden*. Berlin, Germany: de Gruyter, 1978.

[26] A. Marino, I. Hajnsek, and N. Walker, "Validating a ship detector based on the notch filter with RADARSAT-2 fine quad-pol data," in *Proc. SEASAR, Tromsø, Norway*, 2012, pp. 1–31, (ESA SP-709, Sep. 2013).

Ding Tao received the B.E. degree in detection, guidance, and control technology from the Beijing University of Aeronautics and Astronautics, Beijing, China, in 2007 and the M.Sc. degree in remote sensing from the Chalmers University of Technology, Gothenburg, Sweden, in 2010.

In August 2010, he started as a Ph.D. Student Research Fellow with the Department of Physics and Technology, University of Tromsø-The Arctic University of Norway, Tromsø, Norway, where he is also with the Earth Observation Laboratory and the Barents Remote Sensing School. His current research interests focus on investigating remote sensing, maritime target detection, and statistical analysis of sea clutter, particularly with polarimetric synthetic aperture radar images.

Stian Normann Anfinsen (S'06–M'10) received the Cand. Mag. (B.Sc.), Cand. Scient. (M.Phil.), and Ph.D. degrees from the University of Tromsø-The Arctic University of Norway, Tromsø, Norway, in 1997, 2000, and 2010, respectively, all in physics and the M.Sc. degree (with distinction) in communications, control, and digital signal processing from the University of Strathclyde, Glasgow, U.K., in 1998.

From 2001 to 2005, he was with satellite ground station system provider Kongsberg Spacetec, Tromsø. He then moved to the Department of Physics and Technology, University of Tromsø-The Arctic University of Norway, where he is currently an Associate Professor. His current research focuses on statistical modeling, parameter estimation, classification, change detection, and target detection in polarimetric synthetic aperture radar images.

Dr. Anfinsen was recognized as a 2012 Best Reviewer of the IEEE JOURNAL OF SELECTED TOPICS IN APPLIED EARTH OBSERVATIONS AND REMOTE SENSING.

Camilla Brekke (M'12) received the Cand. Scient. and Ph.D. degrees from the University of Oslo, Oslo, Norway, in 2001 and 2008, respectively.

In 2001, she was a System Developer with Ericsson, Asker, Norway. From 2001 to 2002, she was a Young Graduate Trainee with the European Space Agency, Noordwijk, The Netherlands. From 2002 to 2009, she was a Scientist with the Norwegian Defence Research Establishment (FFI), Kjeller, Norway. In 2009, she joined, as an Associate Professor, the Department of Physics and Technology, University of Tromsø-The Arctic University of Norway, Tromsø, Norway, where she is currently with the Earth Observation Laboratory and the Barents Remote Sensing School. From October 2012 to January 2013, she was a Visiting Scientist with the Jet Propulsion Laboratory, Pasadena, CA, USA. Her current research interests include signal and image processing of synthetic aperture radar data for arctic and marine applications.